

DISSIPATION AND HEATING IN SUPERSONIC HYDRODYNAMIC AND MHD TURBULENCE

M. NICOLE LEMASTER AND JAMES M. STONE

Department of Astrophysical Sciences, Princeton University, Princeton, NJ 08544

Draft version October 29, 2018

ABSTRACT

We study energy dissipation and heating by supersonic MHD turbulence in molecular clouds using Athena, a new higher-order Godunov code. We analyze the dependence of the saturation amplitude, energy dissipation characteristics, power spectra, sonic scaling, and indicators of intermittency in the turbulence on factors such as the magnetic field strength, driving scale, energy injection rate, and numerical resolution. While convergence in the energies is reached at moderate resolutions, we find that the power spectra require much higher resolutions that are difficult to obtain. In a 1024^3 hydro run, we find a power law relationship between the velocity dispersion and the spatial scale on which it is measured, while for an MHD run at the same resolution we find no such power law. The time-variability and temperature intermittency in the turbulence both show a dependence on the driving scale, indicating that numerically driving turbulence by an arbitrary mechanism may not allow a realistic representation of these properties. We also note similar features in the power spectrum of the compressive component of velocity for supersonic MHD turbulence as in the velocity spectrum of an initially-spherical MHD blast wave, implying that the power law form does not rule out shocks, rather than a turbulent cascade, playing a significant role in the regulation of energy transfer between spatial scales.

Subject headings: ISM: clouds — ISM: magnetic fields — isothermal — simulations — stars: formation — turbulence

1. INTRODUCTION

Observed non-thermal line widths in molecular clouds (MCs), where all star formation in the Galaxy takes place, point to the presence of supersonic turbulence in such regions (Falgarone & Philips 1990). The properties of the turbulent medium, such as Mach number and magnetic field strength, may determine the products of the star formation process. As an important source of heating within molecular clouds (Stone et al. 1998, hereafter S98), turbulent energy dissipation may also play a role. Much effort has been directed toward numerically simulating turbulent media in order to better understand the link between turbulence and star formation (see Elmegreen & Scalo 2004, MacLow & Klessen 2004, and McKee & Ostriker 2007 and references therein).

As we have not yet identified the turbulent driving mechanism, there remain many unanswered questions about the evolution of molecular clouds. Is the turbulence periodically re-energized, or does it simply decay away? How much impact do magnetic fields have on the properties of the turbulence? Crutcher (1999), using observations of Zeeman splitting, found magnetic fields in some clouds strong enough that one cannot safely neglect their effects. Although it has been shown that magnetic fields do not appreciably lengthen the turbulent decay time (S98; Mac Low 1999), they do create anisotropy within the clouds (e.g. Vestuto et al. 2003, hereafter V03; Esquivel et al. 2003), which may have important observational and evolutionary consequences. For example, molecular clouds are often observed to be filamentary (e.g. Mizuno et al. 1995; Churchwell et al. 2004).

In this paper, we will investigate the energy dissipation properties of supersonic hydrodynamic and MHD

turbulence with a variety of magnetic field strengths using Athena, a new higher-order Godunov code. An important goal of this study is to investigate the effect of the assumed driving mechanism on the properties of the resulting turbulence, such as power spectra and intermittency indicators. Our analysis utilizes data from high-resolution numerical simulations with twenty-five different parameter sets. In recent years, a variety of results have been reported on the properties of supersonic MHD turbulence, including energetics (e.g. S98; Mac Low 1999; Ostriker et al. 2001), power spectra (e.g. Cho & Lazarian 2003, 2005; V03; Padoan et al. 2007, hereafter P07), and probability distribution functions (e.g. Padoan et al. 1997; Passot & Vazquez-Semadeni 1998; Ostriker et al. 2001; Kowal et al. 2007; Kritsuk et al. 2007, hereafter K07). Where possible, we identify differences in our methods and results as compared to those of other groups. In a separate letter (Lemaster & Stone 2008, hereafter Paper I), we have reported the results of an investigation of the variation of the probability distribution function (PDF) of density with Mach number. Our primary result in that paper was that the intermittent behavior of turbulence could be responsible for the large cloud-to-cloud variation in the observed star formation rate per solar mass.

The primary tool available to investigate the properties of highly nonlinear, supersonic MHD turbulence is direct numerical simulation. To date, most results have been computed using a few numerical algorithms, such as ZEUS (e.g. S98; V03; Mac Low 1999; Ostriker et al. 1999; Ostriker et al. 2001), the PENCIL code (e.g. Haugen & Brandenburg 2004), the Stagger code (e.g. P07), and ENO methods (e.g. Cho & Lazarian 2003). There has been concern expressed in the literature that previous results may be strongly affected by numerical dissipa-

tion. Thus, it is worth re-examining the problem with more accurate methods. This study represents one of the first applications of higher-order Godunov methods to the study of supersonic MHD turbulence.

Without knowing the driving mechanism, we are left with many possible methods of generating turbulence in simulations. The hope is that the choice of method for the simulated driving will have an insignificant effect on the results. Federrath, Klessen, & Schmidt (in prep.), however, have shown that compressive and solenoidal forcing produce dramatically different turbulent states. For some diagnostics, such as intermittency, the time-variability of the turbulent state is critical. Even if an array of driving methods produce the same mean state, do the instantaneous states have the same distribution about the mean? We will investigate the dependence on driving scale of various diagnostics, given our particular driving method, which is very similar to that employed by, e.g., S98 and V03.

For power spectra of simulated turbulence to be valuable, the resolution needs to be high enough that the driving and numerical dissipation scales are well separated, allowing the inertial range to be studied. When magnetic fields are taken into account, simulating turbulence at these resolutions can be prohibitively expensive. Another goal of this study is to investigate whether properties of the power spectra and other diagnostics are converged at the numerical resolutions feasible at the moment, up to 1024^3 .

We begin in §2 by describing our numerical methods in detail. We proceed, in §3, to present our results. §3.1 includes a convergence study and Mach number scaling study of saturation amplitudes, §3.2 includes a power spectrum analysis, §3.3 analyzes the sonic scale in 1024^3 runs, and §3.4 considers time-variability and temperature intermittency in the turbulence. Finally, we summarize our results in §4 and discuss the implications.

2. NUMERICAL METHODS

The simulations we present were conducted up to a resolution of 1024^3 with the Athena code (Gardiner & Stone 2005, 2008; Stone et al. 2008; Stone & Gardiner 2008) on a three-dimensional Cartesian grid of length $L = 1$ with periodic boundary conditions. Athena utilizes a higher-order Godunov scheme which exactly conserves mass, momentum, and magnetic flux. We solve the equations of ideal isothermal MHD,

$$\frac{\partial \rho}{\partial t} + \nabla \cdot (\rho \mathbf{v}) = 0, \quad (1)$$

$$\frac{\partial \rho \mathbf{v}}{\partial t} + \nabla \cdot (\rho \mathbf{v} \mathbf{v} - \mathbf{B} \mathbf{B} + P + B^2/2) = 0, \quad (2)$$

and

$$\frac{\partial \mathbf{B}}{\partial t} = \nabla \times (\mathbf{v} \times \mathbf{B}), \quad (3)$$

where $c_s = 1$ and $P = c_s^2 \rho$ are the isothermal sound speed and pressure, respectively. Because our method of driving the turbulence, described in the following paragraph, does not involve modifying the equations of MHD, we include no explicit forcing term here. We use an approximate nonlinear Riemann solver (HLLD; Miyoshi & Kusano 2005) for our MHD runs and an exact nonlinear Riemann solver for our hydrodynamic runs. Both our MHD

and hydro simulations are integrated well past the turbulent saturation time using a directionally-unsplit van Leer scheme (Stone & Gardiner 2008). Further details of how we overcame the numerical difficulties associated with utilizing this method for turbulence can be found in Appendix A.

We initialize a uniform, stationary ambient medium with density $\bar{\rho} = 1$ and magnetic field parallel to the x -axis whose amplitude B_0 is fixed by the value of $\beta = 2c_s^2 \bar{\rho} / B_0^2$. We then apply divergence-free velocity perturbations following a Gaussian random distribution with a Fourier power spectrum of the form

$$|\delta \mathbf{v}_k^2| \propto k^6 \exp(-8k/k_{\text{pk}}) \quad (4)$$

for $kL/2\pi < N/2$, where N is the resolution and k_{pk} is the wavenumber of peak driving, in all but two of our runs. For the remaining two runs, with $\dot{E}/\bar{\rho}L^2c_s^3 = 500$ and $k_{\text{pk}}L/2\pi = 2$ at 1024^3 , we truncate the driving spectrum at $kL/2\pi = 8$. Before applying the perturbations to the grid, we shift them such that no net momentum will be added and normalize them to give the desired energy injection rate, $\dot{E}/\bar{\rho}L^2c_s^3$, or, in the decaying case, initial kinetic energy.

For our driven runs, we choose our energy injection rate to give the desired turbulent Mach number, $\mathcal{M} \equiv \sigma_v/c_s$, in the saturated state. Here, $\sigma_v = [\sigma_{v_x}^2 + \sigma_{v_y}^2 + \sigma_{v_z}^2]^{1/2}$ is the 3D velocity dispersion of the gas and σ_{v_i} is the 1D velocity dispersion in a given direction. The method we use in this paper to compute the turbulent Mach number differs from that used by some other groups; we utilize a density-weighted velocity dispersion, $\sigma_{v_i} = [\langle \rho v_i^2 \rangle / \langle \rho \rangle - (\langle \rho v_i \rangle / \langle \rho \rangle)^2]^{1/2}$. Note that, due to the zero net momentum of our turbulent medium, the second term on the RHS vanishes on the global scale. If we compare the Mach number computed with and without density-weighting the velocity dispersion, we find that the two are fairly correlated, but that the time-average of the latter is $\sim 4\%$ larger than that of the former for driven strong-field MHD turbulence with, e.g., $k_{\text{pk}}L/2\pi = 2$ and $\dot{E}/\bar{\rho}L^2c_s^3 = 500$, or $k_{\text{pk}}L/2\pi = 8$ and $\dot{E}/\bar{\rho}L^2c_s^3 = 1000$. The comparison for the latter case is shown in Figure 1. We will use a density-weighted velocity dispersion for all but our sonic scale analysis.

To drive turbulence in our simulations, we inject energy before each time step, with a new realization of the power spectrum generated at intervals $\Delta t c_s / L = 0.001$. This differs from that done in S98 and V03, where the energy was injected only when a new realization of the spectrum was generated. Ostriker et al. (1999, 2001) and Kowal et al. (2007) used different driving spectra than our own but still constrained their velocity perturbations to be divergence free. Our method differs from that of K07 in that they approximate an isothermal equation of state using an adiabatic index of $\gamma = 1.001$, drive their turbulence on very large scales using an acceleration that is fixed in time, and also allow a substantial fraction of the energy introduced by the forcing to be in compressional modes. P07 also used a fixed acceleration for turbulent driving. It is important to understand if these differences have any significant impact on the results.

For our decaying runs, we again begin with a uniform,

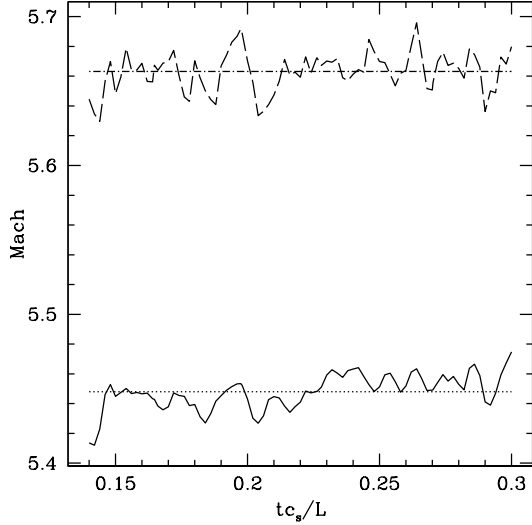


FIG. 1.— Comparison of turbulent Mach number computed with (solid) and without (dashed) density-weighting for the driven, strong-field MHD turbulence with $k_{\text{pk}}L/2\pi = 8$ and $\dot{E}/\bar{\rho}L^2c_s^3 = 1000$. The mean of the latter (dash-dotted) is $\sim 4\%$ higher than that of the former (dotted). With the exception of for our sonic scale analysis, we use density-weighted velocity dispersions.

stationary ambient medium but apply only one driving impulse to the velocity field, with a power spectrum of the same form as is used to initialize our driven runs. We then allow it to evolve undisturbed. We choose the turbulent kinetic energy applied to our medium so as to give the desired initial turbulent Mach number. Our decaying runs differ from those of Sytine et al. (2000), who used a different initial driving spectrum and allowed a compressible component in the initial perturbations. They used an adiabatic equation of state with $\gamma = 1.4$, which we will use only for our decaying simulations. In this case, we solve the total energy equation,

$$\frac{\partial E}{\partial t} + \nabla \cdot \left[(E + P + B^2/2)\mathbf{v} - \mathbf{B}(\mathbf{B} \cdot \mathbf{v}) \right] = 0, \quad (5)$$

in addition to Equations (1)–(3), using the HLLC Riemann solver. Here,

$$E = \frac{P}{\gamma - 1} + \frac{1}{2}\rho v^2 + \frac{1}{2}B^2 \quad (6)$$

with $P = (\gamma - 1)e$ and $B^2 = \mathbf{B} \cdot \mathbf{B}$, where e is the internal energy density and γ is the ratio of specific heats. The numerical methods in Athena conserve total energy exactly.

We primarily investigate strong-field MHD turbulence with $\beta = 0.02$ and hydrodynamic turbulence ($\beta = \infty$), although we present runs with $\beta = 0.2$ (moderate-field) and $\beta = 2.0$ (weak-field) as well. Note that, due to a definition of β in S98 and V03 that differs from ours by a factor of 2, our $\beta = 0.02$ results should be compared to their $\beta = 0.01$ results, and similarly for other values of β . The magnetic fields we use in our simulations correspond to physical values of $B = 2.0 \mu\text{G}\beta^{-1/2}(T/10\text{ K})^{1/2}(n_{\text{H}_2}/10^2\text{ cm}^{-3})^{1/2}$, where T is the temperature and n_{H_2} is the number density of molecular hydrogen. Our simulations are scale-free, allowing them to be scaled to any set of physical parameters using

appropriate choices of $\bar{\rho}$, c_s , and L . Utilizing the same values given in S98, i.e. $L = 2\text{ pc}$, $n_{\text{H}_2} = 10^3\text{ cm}^{-3}$, and $T = 10\text{ K}$, yields energy injection rates of up to $\dot{E} = 0.4L_\odot$, with a magnetic field strength $B = 44\text{ }\mu\text{G}$ for the strong-field case.

3. RESULTS

Figure 2 shows slices in mass density along the far faces of the computational domain for driven $\mathcal{M} = 6.9$ strong-field MHD turbulence with $k_{\text{pk}}L/2\pi = 2$ at 1024^3 . Also included are magnetic field vectors in a slice normal to the y-axis near the bottom of the cube. Due to the strong background magnetic field, the vectors are fairly well aligned. Figure 3 also shows slices in density, but this time for $\mathcal{M} = 7.0$ hydrodynamic turbulence with the same driving scale and resolution. For both cases the structure seen is filamentary, with anisotropy in the scale of the structures in the strong-field case as a result of the field. This is not to say, however, that the filaments are aligned with the magnetic field. In fact, some appear to be oriented perpendicular to the field. Figures 4 and 5 show column density along the line of sight parallel to the z-axis for the same runs as in Figures 2 and 3, respectively. The projected filamentary structure is visible in these column density images. The column density contrast is higher for the strong-field than for the hydrodynamic case.

3.1. Saturation Amplitude

We begin our quantitative analysis by studying the energy in fluctuations once our driven turbulence runs have reached saturation. Since the method with which we drive our turbulence injects energy at a constant rate, at saturation the energy dissipation rate of the turbulence will, on average, equal the energy injection rate. At sufficiently high numerical resolution, the numerical dissipation will become negligible compared to the physically interesting sources of dissipation (shocks), and the energy dissipation properties of the turbulence can give us insight into the heating within and evolution of molecular clouds. In this section, we will first determine the resolution at which the saturation energy has converged, i.e. reached a state such that further increasing the resolution has a negligible effect on the state, for turbulence evolved using Athena and compare the turbulent decay rates to those presented in S98 computed using ZEUS.

The kinetic energy associated with the fluctuations in our turbulent medium can be quantified by $E_K \equiv \int \rho v^2/2 d\mathbf{x}$, where ρ is the density and v is the magnitude of the velocity. An integration for this and all similar quantities is performed over the entire domain. Similarly, the energy in magnetic field perturbations is $\delta E_B \equiv \int (B^2 - B_0^2)/2 d\mathbf{x}$, where B and B_0 are the magnitudes, respectively, of the magnetic field and its initial value. The total energy in perturbations is the sum of the energy in kinetic and magnetic field fluctuations, $E_{\text{pert}} \equiv E_K + \delta E_B$. To analyze the energy dissipation properties of the turbulence, we compute dissipation timescales using $t_{\text{diss}} = E/\dot{E}$, normalizing them to the flow crossing time, $t_f = \lambda_{\text{pk}}/\sqrt{2E_K}$, where $\lambda_{\text{pk}} = 2\pi/k_{\text{pk}}$ is the wavelength of peak driving.

We can partition the kinetic energy by breaking down the velocity into its solenoidal and compressive components. The solenoidal component is divergence-free,

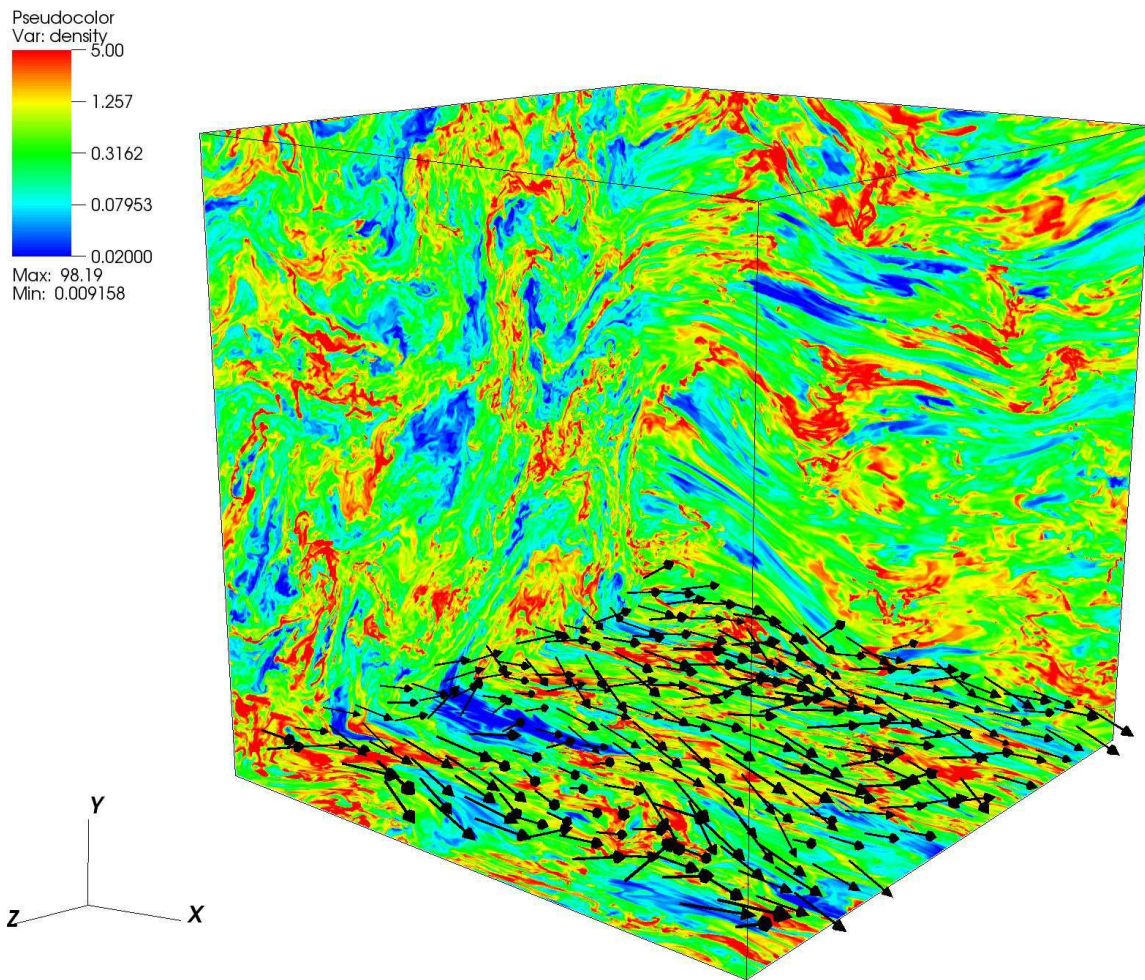


FIG. 2.— Driven strong-field $\mathcal{M} \approx 6.9$ MHD turbulence with $k_{\text{pk}}L/2\pi = 2$ at 1024^3 . Slices of density along the far faces of the cube on a logarithmic color scale from 0.02 (blue) to 5.0 (red). Magnetic field vectors along a slice normal to the y -axis at $y \approx 0.0625$ are fairly well aligned and there is anisotropy in the scale of the structures that results from the magnetic field.

whereas the compressive component is curl-free. These can easily be computed using $\mathbf{v}_C(\mathbf{k}) = [\hat{k} \cdot \mathbf{v}(\mathbf{k})]\hat{k}$ and $\mathbf{v}_S(\mathbf{k}) = [\hat{k} \times \mathbf{v}(\mathbf{k})] \times \hat{k}$, respectively. For simulations with comparable parameters (i.e. $k_{\text{pk}}L/2\pi = 8$ and $\dot{E}/\bar{\rho}L^2c_s^3 = 1000$), these energies can be compared directly with the values given in S98 and V03 after accounting for the difference in definition of β . We average our quantities over at least one dynamical time, often several, beginning after the turbulence has fully saturated.

To determine the rate of convergence of a given volume-integrated quantity, q , we compute the percent error in the quantity at each resolution relative to the converged value. In the case where the quantity changes monotonically with resolution, we find the converged value by performing a three-parameter fit, $(q_N - q_\infty)/q_\infty = cN^{-\alpha}$, where N is the resolution and q_N is the value at that resolution. The results of this fit tell us (1) the converged value, q_∞ , (2) the order of convergence, α , and (3) the coefficient, c , that determines the resolution at which our result has converged, i.e. when $(q_N - q_\infty)/q_\infty < 0.01$.

3.1.1. Hydrodynamic Convergence Study

To determine the resolution at which our numerical dissipation has become small compared to shock dis-

sipation, we analyze the properties of driven, supersonic hydrodynamic turbulence at resolutions from 32^3 to 512^3 . We study two sets of simulations with identical energy injection rate, $\dot{E}/\bar{\rho}L^2c_s^3 = 1000$, but differing driving scales. The set of runs with small-scale driving, $k_{\text{pk}}L/2\pi = 8$, correspond to the hydrodynamic run in S98, while the other set of runs are driven at twice the scale, $k_{\text{pk}}L/2\pi = 4$. The properties of the 512^3 run from each set can be found in Table 1. We have not performed a convergence study of the $k_{\text{pk}}L/2\pi = 2$ runs due to the high level of time-variability (discussed in §3.4.1).

Although both sets of runs are driven with energy injection rate $\dot{E}/\bar{\rho}L^2c_s^3 = 1000$, the larger driving scale of the $k_{\text{pk}}L/2\pi = 4$ set causes it to converge to $\mathcal{M} \approx 7.2$, while the $k_{\text{pk}}L/2\pi = 8$ set converges to only $\mathcal{M} \approx 5.8$. The former set reaches convergence by 64^3 , with higher resolutions having a small scatter about the converged value. The latter set, on the other hand, converges monotonically at order $\alpha \approx 1.6$ for all resolutions analyzed, reaching within 1% of the converged value by 128^3 .

The kinetic energy in fluctuations of the set with larger driving scale, $k_{\text{pk}}L/2\pi = 4$, converges to a value of $E_K \approx 26$ by 64^3 and has some scatter about the converged value for higher resolutions. For the set with smaller driving

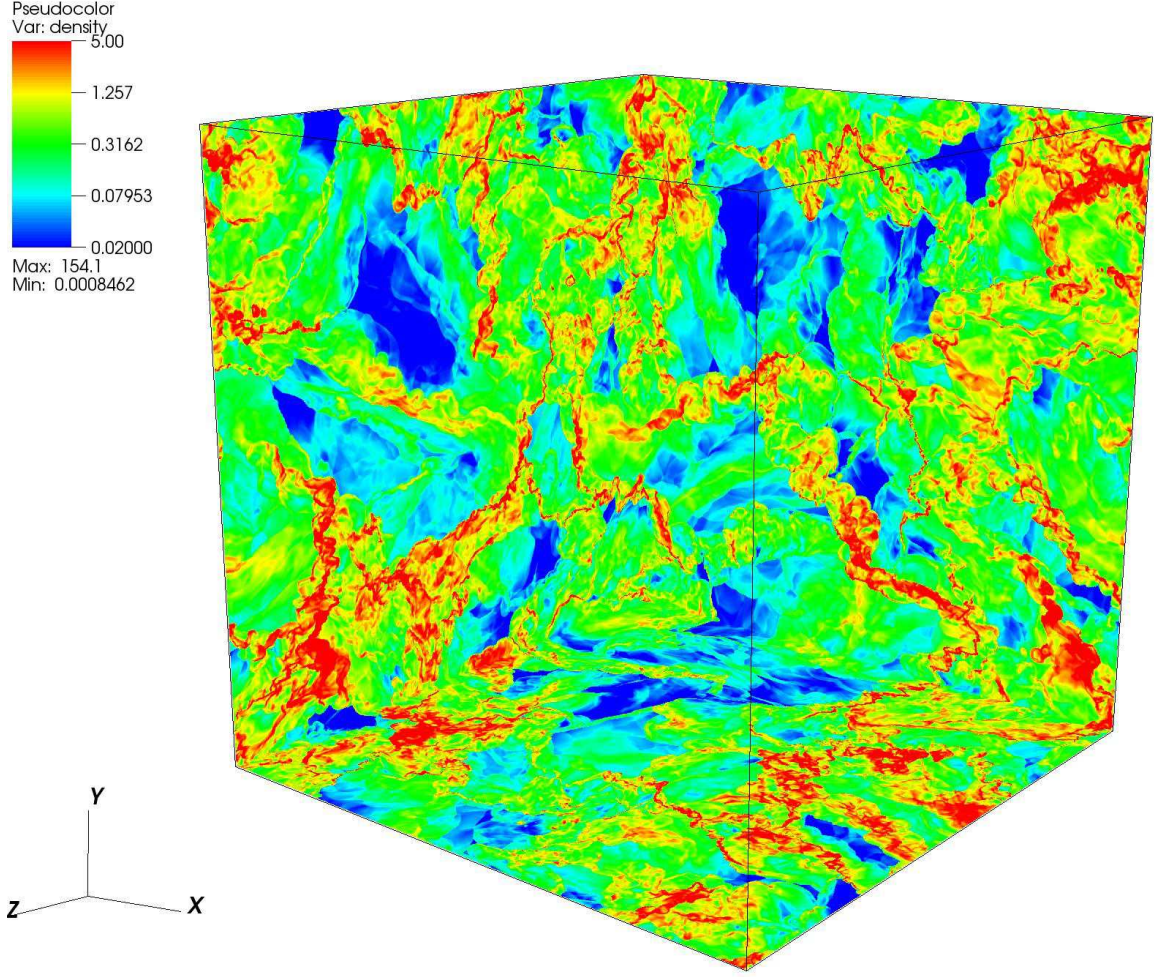


FIG. 3.— Driven $\mathcal{M} \approx 7.0$ hydrodynamic turbulence with $k_{\text{pk}}L/2\pi = 2$ at 1024^3 . Slices of density along the far faces of the cube on a logarithmic color scale from 0.02 (blue) to 5.0 (red). The structures in this case are isotropic.

TABLE 1
DRIVEN HYDRO TURBULENCE AT 512^3

$k_{\text{pk}}L/2\pi$	$\dot{E}/\bar{\rho}L^2c_s^3$	\mathcal{M}	E_K	E_C	E_S	t_{diss}/t_f	σ_E/E	$\sigma_{Q,V}/Q_V$	$\sigma_{Q,M}/Q_M$
8	1000	5.8	17	3.8	13	0.77	< 1%	—	—
4	1000	7.2	26	5.9	20	0.76	1%	1%	2%
4	375	5.3	14	3.1	11	0.78	1%	1%	2%
4	140	3.8	7.2	1.6	5.6	0.78	1%	2%	2%
4	40	2.6	3.3	0.7	2.6	0.84	1%	< 1%	< 1%
4	3.5	1.2	0.8	0.1	0.7	1.1	< 1%	< 1%	< 1%
2	500	7.0	25	5.5	19	0.7	4%	2%	4%
2	187.5	5.2	13	3.1	10	0.73	2%	1%	4%
2	70	3.7	6.9	1.6	5.4	0.74	2%	2%	2%
2	20	2.5	3.1	0.6	2.5	0.77	1%	3%	3%
2	1.75	1.2	0.7	0.1	0.6	0.99	2%	4%	4%

scale, $k_{\text{pk}}L/2\pi = 8$, the kinetic energy in fluctuations converges at order $\alpha \approx 1.5$ to only $E_K \approx 17$. The value at 128^3 is within 2% of the converged value, while at 256^3 it is within a fraction of a percent.

Although we have an extremely low sampling rate for the fraction of the kinetic energy in solenoidal and compressive modes, they appear to be independent of driving scale. The solenoidal fraction converges to $E_S/E_K \approx 0.78$, decreasing with increasing resolution, while the compressive fraction converges to $E_C/E_K \approx 0.22$. The

solenoidal fraction is within a fraction of a percent of the converged value by 256^3 ; however, it varies by only a small amount down to low resolution. Finally, the ratio of the energy dissipation timescale to the flow crossing time at the driving scale increases with resolution, to $t_{\text{diss}}/t_f \approx 0.78$ for the $k_{\text{pk}}L/2\pi = 4$ set and $t_{\text{diss}}/t_f \approx 0.76$ for the $k_{\text{pk}}L/2\pi = 8$ set, only a small difference. Consistent with our previous results, the $k_{\text{pk}}L/2\pi = 4$ set converges at lower resolution than the $k_{\text{pk}}L/2\pi = 8$ set, 64^3 and 256^3 , respectively. The turbulence dissipates in

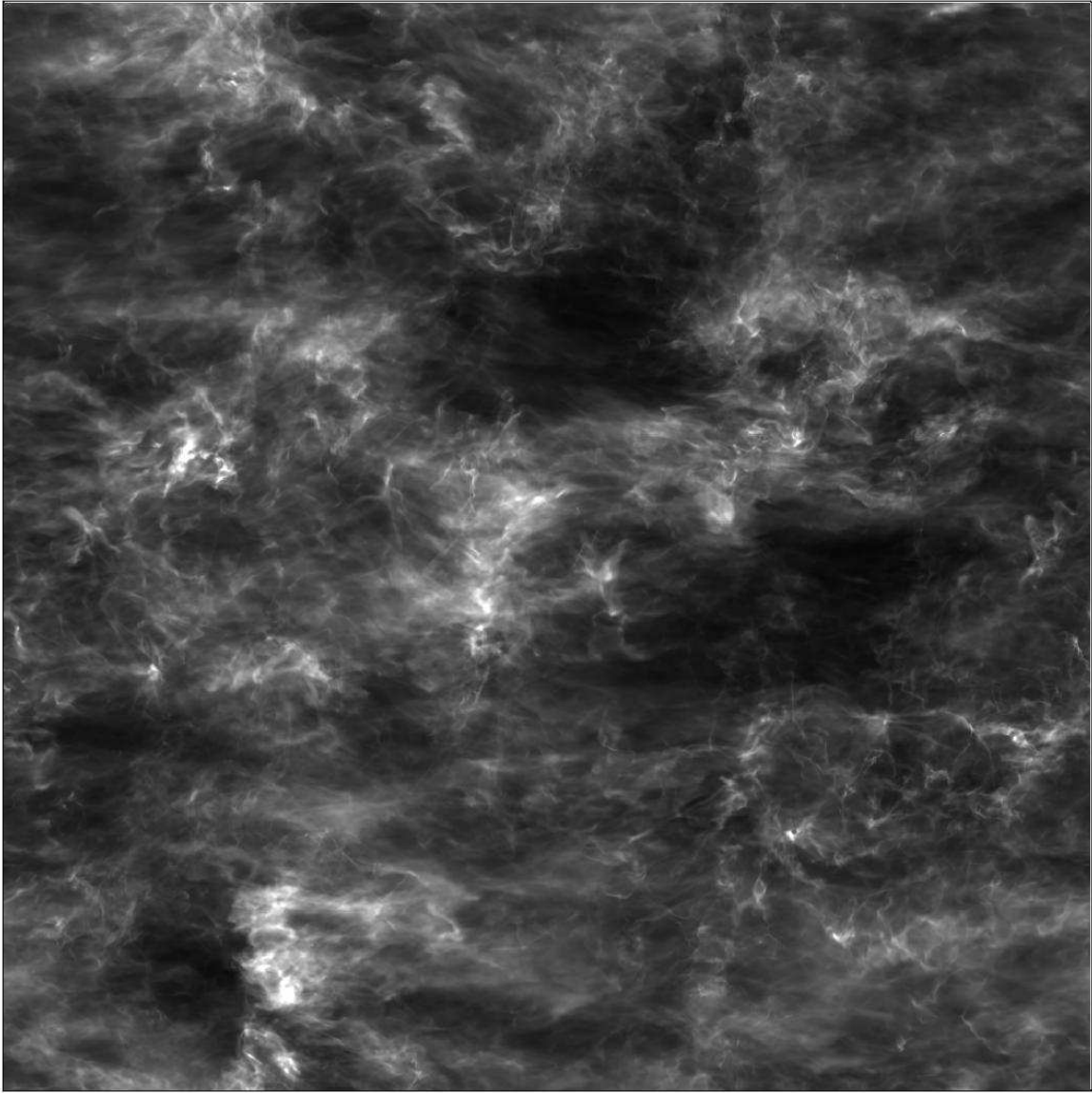


FIG. 4.— Column density along line of sight parallel to z -axis for driven strong-field MHD turbulence with $k_{\text{pk}}L/2\pi = 2$ at 1024^3 on a linear gray scale from 0.3 (black) to 3.4 (white).

less than a flow crossing time in all cases.

Although the converged Mach number and saturation energies are higher for $k_{\text{pk}}L/2\pi = 4$ than for $k_{\text{pk}}L/2\pi = 8$, the fraction of the energy in the solenoidal or compressive mode, as well as the ratio of the energy dissipation timescale to the flow crossing time at the driving scale, are relatively independent of the driving scale. While most of the quantities of interest converge between 128^3 and 256^3 for the $k_{\text{pk}}L/2\pi = 8$ hydrodynamic runs, convergence has already been reached for these quantities by 64^3 for the $k_{\text{pk}}L/2\pi = 4$ runs. High resolutions are critical for separating the driving and dissipation scales in the power spectra far enough to study the inertial range; however, quantities such as energy dissipation rate and turbulent Mach number converge at resolutions which are more easily attainable.

3.1.2. MHD Convergence Study

We now analyze driven, strong-field, supersonic MHD turbulence in the same manner as in the previous section.

To determine the resolution at which our numerical dissipation becomes negligible, we study the convergence of two sets of MHD simulations with energy injection rate $\dot{E}/\bar{\rho}L^2c_s^3 = 1000$ at resolutions from 32^3 to 512^3 . One set has $k_{\text{pk}}L/2\pi = 8$, similar to the strong-field MHD run in S98, while the other has $k_{\text{pk}}L/2\pi = 4$. The properties of the 512^3 run from each set can be found in Table 2. Again, we have not performed a convergence study of the $k_{\text{pk}}L/2\pi = 2$ runs due to the high level of time-variability (discussed in §3.4.1).

As in the hydrodynamic case, the $k_{\text{pk}}L/2\pi = 4$ MHD runs converge to a higher Mach number, $\mathcal{M} \approx 6.8$, than the $k_{\text{pk}}L/2\pi = 8$ runs ($\mathcal{M} \approx 5.5$). The former is converged by 256^3 , while the latter converges at 1st order, only reaching convergence at 512^3 . The total energy in fluctuations converges at nearly 1st order to $E_{\text{pert}} \approx 36$ for $k_{\text{pk}}L/2\pi = 4$, shown in Figure 6. While convergence has definitely been reached by 512^3 , the 256^3 value is less than 2% from the converged value. For $k_{\text{pk}}L/2\pi = 8$, on

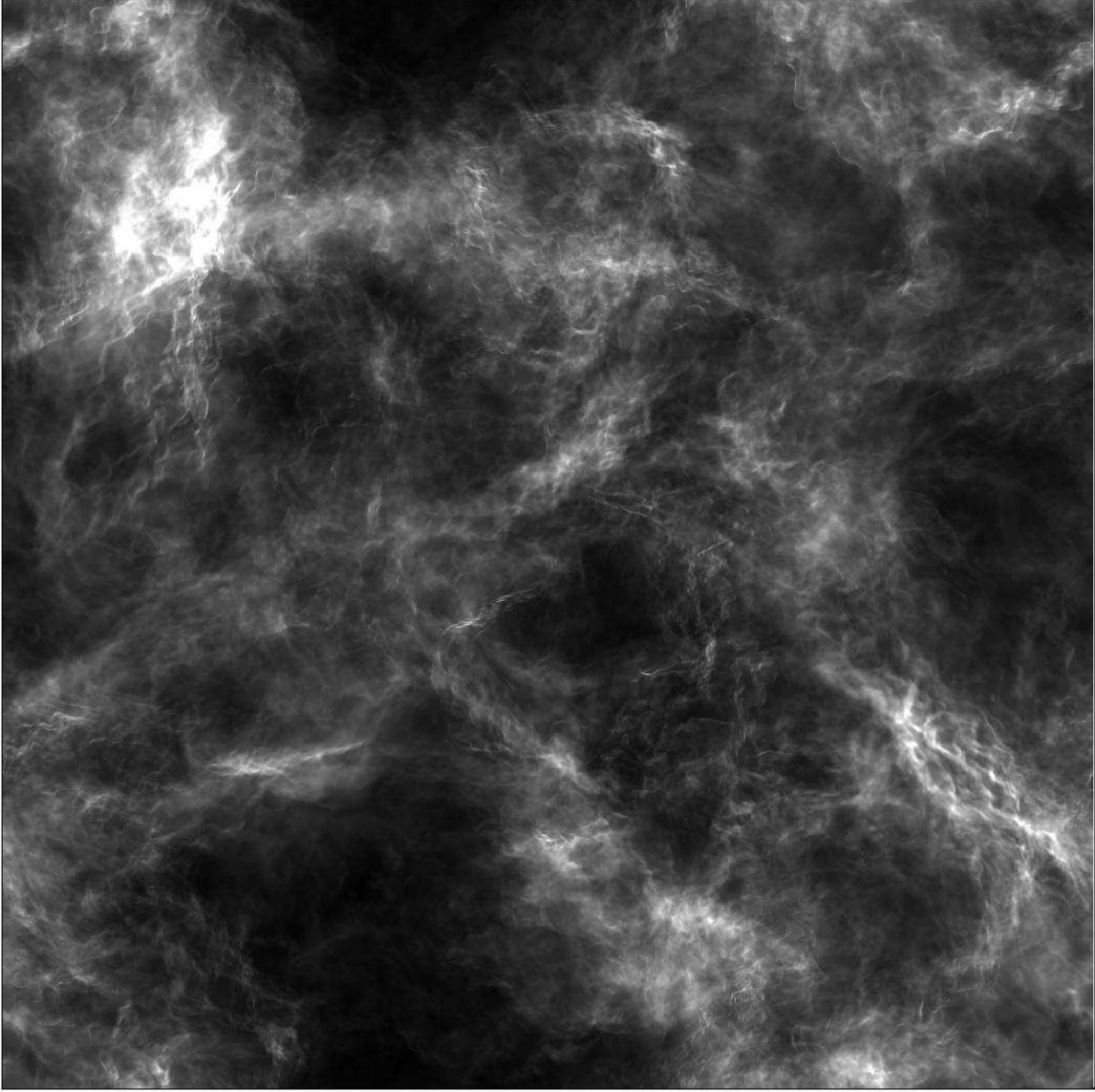


FIG. 5.— Column density along line of sight parallel to z -axis for driven hydrodynamic turbulence with $k_{\text{pk}}L/2\pi = 2$ at 1024^3 on a linear gray scale from 0.3 (black) to 3.4 (white).

TABLE 2
DRIVEN MHD TURBULENCE AT 512^3

β	$k_{\text{pk}}L/2\pi$	$\dot{E}/\bar{\rho}L^2c_s^3$	\mathcal{M}	E_K	E_C	E_S	E_B	$t_{\text{diss}}/t_{\text{f}}$	σ_E/E	$\sigma_{Q,V}/Q_V$	$\sigma_{Q,M}/Q_M$
2.0	8	1000	5.3	14	2.1	12	5.8	0.83	< 1%	—	—
0.2	8	1000	5.1	13	1.6	11	8.6	0.89	< 1%	—	—
0.02	8	1000	5.4	15	1.5	13	8.2	1.0	< 1%	—	—
0.02	4	1000	6.8	23	2.3	21	13	0.98	< 1%	1%	2%
0.02	4	375	5.2	14	1.1	13	6.4	1.1	< 1%	< 1%	2%
0.02	4	140	3.8	7.3	0.5	6.7	3.1	1.1	3%	2%	< 1%
0.02	4	40	2.7	3.6	0.2	3.4	1.4	1.3	< 1%	3%	3%
0.02	4	3.5	1.3	0.8	0.04	0.8	0.3	1.7	< 1%	2%	2%
0.02	2	500	7.0	24	2.2	22	11	0.98	4%	4%	5%
0.02	2	187.5	5.0	13	1.2	11	5.9	0.99	3%	2%	2%
0.02	2	70	3.7	6.8	0.6	6.3	2.9	1.0	3%	4%	5%
0.02	2	20	2.5	3.1	0.2	2.9	1.3	1.1	2%	3%	4%
0.02	2	1.75	1.2	0.8	0.06	0.7	0.4	1.6	6%	9%	8%

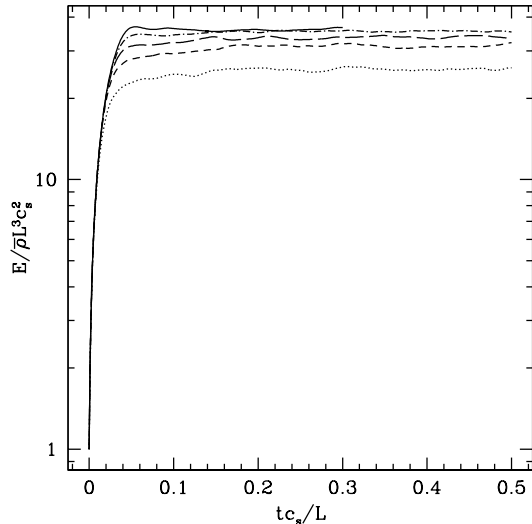


FIG. 6.— Total energy in fluctuations in driven MHD turbulence runs with $k_{\text{pk}}L/2\pi = 4$ at 32^3 (dotted), 64^3 (short dashed), 128^3 (long dashed), 256^3 (dash dotted), and 512^3 (solid). The saturated energy has converged by 256^3 .

the other hand, convergence is not reached until 512^3 , where $E_{\text{pert}} \approx 23$. Convergence is at nearly 1st order for this case as well.

For the energy in magnetic field perturbations, convergence is reached at 512^3 for both the $k_{\text{pk}}L/2\pi = 4$ and $k_{\text{pk}}L/2\pi = 8$ cases. Convergence is approached at roughly 0.7 order for both cases. The fraction of the total energy (magnetic plus kinetic) in magnetic field fluctuations increases with resolution, reaching 35% at 512^3 . When driven at $k_{\text{pk}}L/2\pi = 4$, the kinetic energy in fluctuations converges to $E_K \approx 23$ by around 256^3 , while at $k_{\text{pk}}L/2\pi = 8$ it converges at order 0.9 to $E_K \approx 15$ by 512^3 .

The fraction of the kinetic energy fluctuations in solenoidal modes increases with resolution for both the $k_{\text{pk}}L/2\pi = 4$ and $k_{\text{pk}}L/2\pi = 8$ cases, converging to $E_S/E_K \approx 0.9$. The fraction in compressive modes, on the other hand, decreases with resolution to $E_C/E_K \approx 0.1$. Convergence for these quantities is not reached until 512^3 . Finally, the ratio of the dissipation timescale to the flow crossing time at the driving scale converges to $t_{\text{diss}}/t_f \approx 0.98$ by 256^3 for $k_{\text{pk}}L/2\pi = 4$, while for $k_{\text{pk}}L/2\pi = 8$ it converges to $t_{\text{diss}}/t_f \approx 1.0$ by 512^3 . Even with a strong magnetic field, the turbulence dissipates in a flow crossing time.

Just as in the hydrodynamic case, the increased driving scale caused a higher turbulent Mach number and energy at saturation for the $k_{\text{pk}}L/2\pi = 4$ than for the $k_{\text{pk}}L/2\pi = 8$ case. The fraction of the kinetic energy in solenoidal or compressive modes, however, was independent of driving scale, just as before. The ratio of the dissipation timescale to flow crossing time was also relatively independent of the driving scale. Convergence for strong-field MHD turbulence was reached at higher resolutions, typically 512^3 , than for hydrodynamic turbulence.

3.1.3. Comparison to ZEUS

Because we performed a convergence study using the same turbulence parameters as in S98, we can directly compare our high-resolution results to those published therein. For driven strong-field MHD turbulence with $k_{\text{pk}}L/2\pi = 8$, we find at 256^3 that our total energy in fluctuations at saturation is only 8% higher than that found in S98, due to the lower level of numerical dissipation at this resolution in Athena than in ZEUS. For intermediate- and weak-field MHD, our energies are 7% and 8% higher, respectively. It is likely that neither our results nor the S98 results have converged by this resolution, however.

At 512^3 , there is no obvious difference between the total energy in fluctuations for our strong-field MHD simulation and the S98 result. The values from these two codes converge, even though they utilize completely different numerical methods. The ratio of magnetic to kinetic energy fluctuations, however, is different for the two codes, yielding ratios of dissipation timescale to flow crossing time that differ more substantially. At 256^3 , this ratio is 14% greater for our strong-field MHD run than that presented in S98. For intermediate- and weak-field MHD, our ratios are both 11% greater. In all cases, the ratio of timescales remains below unity.

For our driven hydro run at 256^3 with $k_{\text{pk}}L/2\pi = 8$, we find that our total energy in fluctuations at saturation is also only 8% higher than that found in S98. Although our result has converged by this resolution, the ZEUS result may not yet be converged. The ratio of dissipation timescale to flow crossing time in this case is 11% greater than that found in S98, but is still below unity. Although it has been suggested in the literature that the rapid decay of supersonic turbulence is due to excessive numerical dissipation in ZEUS, these results, computed with a higher-order Godunov scheme, do not support that conclusion.

3.1.4. Hydrodynamic Mach Number Scaling

To investigate the effect of the turbulent Mach number on energies and dissipation rates in the turbulence, we now analyze two series of five driven, supersonic hydrodynamic turbulence simulations at 512^3 . One series is driven at $k_{\text{pk}}L/2\pi = 4$, while the other is driven at a larger scale of $k_{\text{pk}}L/2\pi = 2$. The energy injection rates of the latter series, the same that we use in Paper I, are half that of the former series, giving roughly equal Mach numbers to the corresponding pairs. These Mach numbers all fall within the range $1.2 \leq \mathcal{M} \leq 7.2$. The properties of these runs can be found in Table 1.

The kinetic energy in each series of runs spans 1.5 orders of magnitude. We find a power law relationship between the kinetic energy and energy injection rate, i.e.

$$E_K \approx 0.49[(k_{\text{pk}}L/2\pi)/2]^{-1/2}(\dot{E}/\bar{\rho}L^2c_s^3)^{0.62}. \quad (7)$$

The relationship between the kinetic energy and Mach number is, of course, exactly $E_K = 0.5\mathcal{M}^2$ since our Mach numbers are computed from the *density-weighted* velocity dispersion and there is no net momentum associated with the turbulent medium as a whole. We find for our driving method that we can estimate the Mach number that will result from a given energy injection rate using

$$\mathcal{M} \approx 0.99[(k_{\text{pk}}L/2\pi)/2]^{-1/4}(\dot{E}/\bar{\rho}L^2c_s^3)^{0.31}. \quad (8)$$

While this equation gives an indication of how the dissipation scales with Mach number, the exact relations will only apply to our unique driving method.

For the runs driven at $k_{\text{pk}}L/2\pi = 4$, the fraction of the kinetic energy in compressive modes varies by only a fraction of a percent among the runs with $3.8 \leq \mathcal{M} \leq 7.2$. These runs have $E_C/E_K \approx 0.22$. The fraction drops off only slightly for the $\mathcal{M} = 2.6$ run, but then drops substantially, to $E_C/E_K \approx 0.14$, for the $\mathcal{M} = 1.2$ run. For the runs driven at $k_{\text{pk}}L/2\pi = 2$, the fraction for the $\mathcal{M} = 7.0$ and $\mathcal{M} = 3.7$ runs is also $E_C/E_K \approx 0.22$, while the $\mathcal{M} = 5.2$ and $\mathcal{M} = 2.5$ runs have a bit larger and smaller fractions, respectively. Once again, the fraction for the $\mathcal{M} = 1.2$ run is substantially smaller, $E_C/E_K \approx 0.15$. It appears as though the fraction of the energy in compressive modes remains roughly the same except when the turbulence is only mildly supersonic, where the fraction is much lower.

The ratio of the dissipation timescale to the flow crossing time at the driving scale remains below unity for all except the $\mathcal{M} = 1.2$ run at $k_{\text{pk}}L/2\pi = 4$. While the ratio for the runs at $k_{\text{pk}}L/2\pi = 4$ with $\mathcal{M} \geq 3.8$ doesn't vary much, when we increase the driving scale to $k_{\text{pk}}L/2\pi = 2$ the value does change with Mach number. The ratio for the $k_{\text{pk}}L/2\pi = 4$ runs is always larger for a given Mach number than is the ratio for the $k_{\text{pk}}L/2\pi = 2$ runs.

3.1.5. MHD Mach Number Scaling

Finally, we analyze two series of five driven, supersonic, strong-field MHD turbulence simulations at 512^3 to determine the effect of the turbulent Mach number on the energies and dissipation rates. As before, one series is the same $k_{\text{pk}}L/2\pi = 2$ set of runs used in Paper I, while the other is driven at $k_{\text{pk}}L/2\pi = 4$ with twice the energy injection rate, yielding pairs of simulations of roughly the same Mach number within the range $1.2 \leq \mathcal{M} \leq 7.0$. The properties of these runs can be found in Table 2.

As in the hydro case, the kinetic energy in each strong-field MHD series spans nearly 1.5 orders of magnitude. The total energy in fluctuations, which also includes the energy in magnetic field perturbations, increases by an even larger amount from the lowest to highest Mach number runs. The power law relationship between the Mach number and energy injection rate is

$$\mathcal{M} \approx (1.04 \pm 0.02)[(k_{\text{pk}}L/2\pi)/2]^{-1/4}(\dot{E}/\bar{\rho}L^2c_s^3)^{0.30}, \quad (9)$$

which leads to a slightly narrower range of Mach numbers than does the relation for pure hydro. Again, although this gives an indication of how energy dissipation scales with Mach number, the exact relationship is unique to our driving method.

The fraction of the kinetic energy in compressive modes for strong-field MHD is much less than for hydro. When $k_{\text{pk}}L/2\pi = 2$, the fractions increase monotonically with Mach number, from only $E_C/E_K \approx 0.05$ for $\mathcal{M} = 1.3$ to $E_C/E_K \approx 0.10$ for $\mathcal{M} = 6.8$. When $k_{\text{pk}}L/2\pi = 4$, however, the values are much less predictable. In this case, the $\mathcal{M} = 3.7$ and $\mathcal{M} = 1.2$ runs have nearly identical values when $k_{\text{pk}}L/2\pi = 2$, whereas for hydro the fraction at low Mach number was substantially smaller than the values for higher Mach numbers.

The ratio of the dissipation timescale to the flow crossing time at the driving scale decreases with Mach number. While the values for high Mach number are below

unity, the low Mach number values become as large as $t_{\text{diss}}/t_f \approx 1.7$. The values for the highest Mach numbers are roughly the same for both driving scales, but for the smaller driving scale they increase more quickly. The Mach number has a strong influence on the dissipation rate of the turbulence, but even for $\mathcal{M} \approx 1.2$ the dissipation timescale does not exceed twice the flow crossing time.

3.2. Power Spectra

We next consider turbulent velocity power spectra. We compute the power spectrum (PS) of the velocity, $P_K(\mathbf{k}) = |\mathbf{v}(\mathbf{k})|^2/2$, as well as that of its compressive and solenoidal components, $P_C(\mathbf{k}) = |\hat{\mathbf{k}} \cdot \mathbf{v}(\mathbf{k})|^2/2$ and $P_S(\mathbf{k}) = |\hat{\mathbf{k}} \times \mathbf{v}(\mathbf{k})|^2/2$, respectively, in the same way as was done in V03 for the PSD of the specific kinetic energy and its components. To generate the spherically-integrated compensated power spectra that we will present, we average $P(\mathbf{k})$ within spherical shells and multiply by the volume within the shell, $dV = 4\pi k^2 dk$, to find $P(k)$, where $k = (k_x^2 + k_y^2 + k_z^2)^{1/2}$.

To determine the degree of anisotropy in MHD turbulence, we will also analyze cylindrically-integrated power spectra. We generate these spectra by averaging $P_K(\mathbf{k})$ over cylindrical shells whose axes are oriented along the mean magnetic field direction. This yields $P_K(k_{\parallel}, k_{\perp})$, where $k_{\parallel} = |k_x|$ is parallel to the mean magnetic field and $k_{\perp} = (k_y^2 + k_z^2)^{1/2}$ is in the plane normal to the field.

The majority of the power spectra we present in our figures are compensated—divided by a power law to produce plots where the inertial range is very roughly horizontal, making small deviations from a power law easier to see. For each of our driven turbulence runs, we compute power spectra from many snapshots taken at regular intervals, averaging them together to minimize the effects of rare events. With the exception of the 1024^3 runs, we average over at least 69 snapshots spanning at least 4.6 dynamical times. While we averaged over 2.7 dynamical times for the 1024^3 hydro run, the MHD case is not sufficiently time-averaged.

3.2.1. Decaying Subsonic Hydrodynamic Turbulence

Sytine et al. (2000) presented the power spectra of decaying, subsonic, adiabatic hydrodynamic turbulence at a range of resolutions. These power spectra demonstrate the formation of a feature known as the bottleneck effect. Energy cascades down from larger scales but cannot easily be dissipated, causing a build-up of small-scale power. We begin by verifying that Athena can reproduce the bottleneck. These are the only set of adiabatic runs we will consider.

The initial velocity perturbations in these decaying runs have the same form of power spectrum as in our driven runs with $k_{\text{pk}}L/2\pi = 4$ and are normalized to give an initial turbulent Mach number of $\mathcal{M}_0 = 0.5$. After this impulse is given to the initially uniform ambient medium, it is allowed to evolve undisturbed until $tc_s/L = 2$. Figure 7 shows the uncompensated velocity power spectrum at this time for runs with resolutions from 256^3 to 1024^3 . As expected, this plot appears very similar to Figure 11 of Sytine et al. (2000). Since Athena was designed to have low numerical dis-

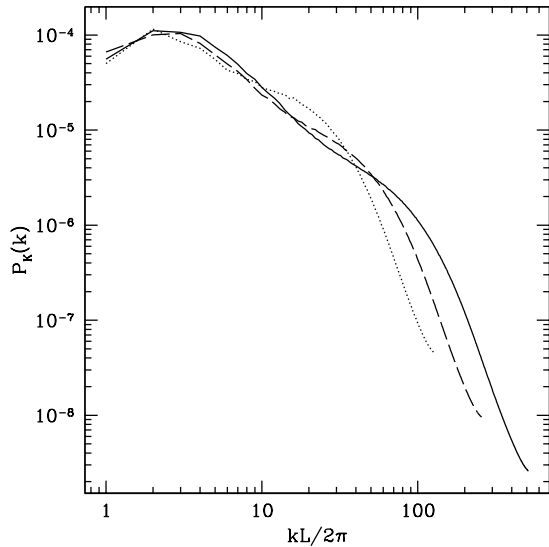


FIG. 7.— Spherically-integrated velocity power spectra at $tc_s/L = 2$ for decaying initially Mach 0.5 adiabatic hydro turbulence with $k_{pk}L/2\pi = 4$, at 1024^3 (solid), 512^3 (long dashed), and 256^3 (dotted). Compare to Figure 11 of Sytine et al. (2000).

sipation, the bottleneck is strong in our simulations of mildly-compressible (subsonic) turbulence.

Analyzing the compressive and solenoidal components of the velocity separately, we find that the bottleneck appears quite strong in the PS of the latter while apparently absent in that of the former. This is not surprising as shocks directly couple large and small scales, allowing the compressive energy to bypass the turbulent cascade and be immediately dissipated. The absence of the bottleneck in the compressive component agrees with the results of Porter et al. (1999) for Mach 1 driven, adiabatic hydro turbulence. At the very highest wavenumbers in our simulations, the power in the compressive component flattens out. Although this could be an artifact of the code related to its treatment of shocks, one should be wary of putting too much stock in the high- k region of any power spectrum as effects such as aliasing (introduced in the calculation of the power spectrum, not the fluid dynamics) could substantially alter the power in that region (see, e.g., Press et al. 1992 for a more detailed discussion).

3.2.2. Driven Hydrodynamic Turbulence

Next we consider driven supersonic (isothermal) hydrodynamic turbulence. We compute velocity power spectra for runs with $k_{pk}L/2\pi = 2$ to maximize the separation between the driving and dissipative scales. To obtain a slightly higher turbulent Mach number, $\mathcal{M} \approx 7.0$, than before, we use an energy injection rate of $\dot{E}/\bar{\rho}L^2c_s^3 = 500$. These are the same runs from the Mach number scaling analysis of §3.1.4.

Figure 8 shows our compensated time-averaged velocity power spectrum for resolutions of 256^3 through 1024^3 . To align the dissipative range for simulations with different resolutions, we express wavenumber as a fraction of the Nyquist value, $k_N L/2\pi = N/2$ for a simulation with resolution N^3 . At low resolution we see no inertial range, but by 1024^3 we have separated the driving and dissipative scales enough that we may be just start-

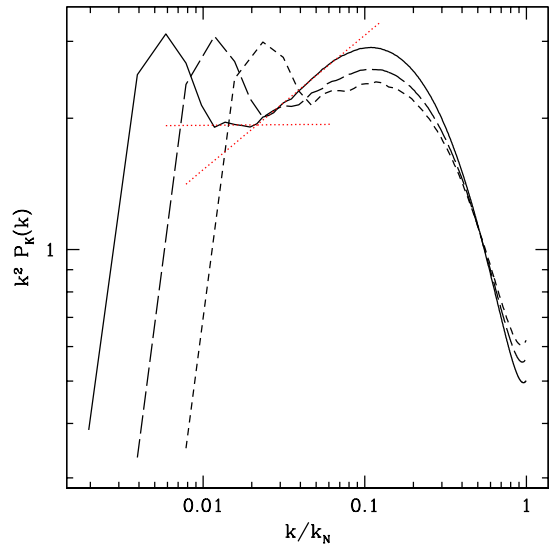


FIG. 8.— Spherically-integrated, compensated power spectra of velocity for driven hydro turbulence runs with $k_{pk}L/2\pi = 2$ at 1024^3 (solid), 512^3 (long dashed), and 256^3 (short dashed). The x-axis has been renormalized to give $k/k_N = 1$. Also shown are fits (dotted) to the slope of the 1024^3 run over the ranges $6 \leq kL/2\pi \leq 11$ and $11 \leq kL/2\pi \leq 36$, representing power laws $P(k) \propto k^{-2.00}$ and $P(k) \propto k^{-1.69}$, respectively.

ing to see an inertial range. There is a small range, $6 \leq kL/2\pi \leq 11$, where we see roughly a $P(k) \propto k^{-2}$ power law, but we are still using a small amount of forcing up through $kL/2\pi = 8$ so the slope in this range may be affected. We find a much longer power law range over $11 \leq kL/2\pi \leq 36$, $P(k) \propto k^{-1.7}$. Although it may be argued that a slope this shallow must be due to a bottleneck, the range of scales with steeper slope is far too limited to conclude this definitively from our data. A higher resolution would be required to determine if this is actually the case.

Figures 9 and 10 show power spectra of the solenoidal and compressive components of velocity, respectively. For the solenoidal component, we find power laws $P(k) \propto k^{-2.0}$ and $P(k) \propto k^{-1.6}$ over the ranges $6 \leq kL/2\pi \leq 11$ and $11 \leq kL/2\pi \leq 36$, respectively. For the compressive component, however, we find only $P(k) \propto k^{-1.8}$ over the range $10 \leq kL/2\pi \leq 40$. In two independent 512^3 simulations that use different random perturbations to seed and drive the turbulence, we find the slopes of the compressive component to agree with each other as well as that of the 1024^3 simulation to within a percent, suggesting that the length of our time-averaging is sufficient. The ratio of power in the compressive and solenoidal components of velocity is much higher than for subsonic turbulence, having the effect of slightly washing out the shallow feature in the velocity spectrum in the supersonic case.

When comparing hydro turbulence with $k_{pk}L/2\pi = 8$, we find more power at high wavenumbers for turbulence evolved using Athena than using ZEUS. Although it was stated in V03 that the bottleneck would not affect finite difference codes, plotting the compensated power spectrum shows some evidence of blending of the driving peak with a secondary bump or shallowing of the spectrum (much less prominent than in our own). If this is

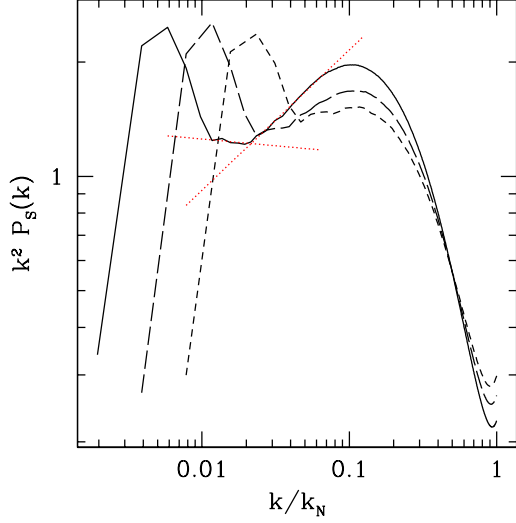


FIG. 9.— Spherically-integrated, compensated power spectra of the solenoidal component of velocity for driven hydro turbulence runs with $k_{\text{pk}}L/2\pi = 2$ at 1024^3 (solid), 512^3 (long dashed), and 256^3 (short dashed). The x-axis has been renormalized to give $k/k_N = 1$. Also shown are fits (dotted) to the slope of the 1024^3 run over the ranges $6 \leq kL/2\pi \leq 11$ and $11 \leq kL/2\pi \leq 36$, representing power laws $P(k) \propto k^{-2.04}$ and $P(k) \propto k^{-1.63}$, respectively.

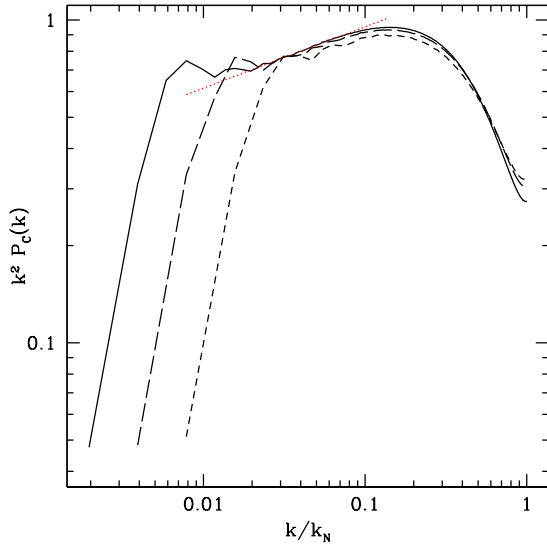


FIG. 10.— Spherically-integrated, compensated power spectra of the compressive component of velocity for driven hydro turbulence runs with $k_{\text{pk}}L/2\pi = 2$ at 1024^3 (solid), 512^3 (long dashed), and 256^3 (short dashed). The x-axis has been renormalized to give $k/k_N = 1$. Also shown is a fit (dotted) to the slope of the 1024^3 run over the range $10 \leq kL/2\pi \leq 40$, representing the power law $P(k) \propto k^{-1.81}$.

indeed a bottleneck, this difference likely results from the greater numerical dissipation in ZEUS than in Athena.

3.2.3. Driven MHD Turbulence

Analyzing driven strong-field MHD turbulence with $k_{\text{pk}}L/2\pi = 2$ and an energy injection rate of $\dot{E}/\bar{\rho}L^2c_s^3 = 500$, shown in Figure 11, we again find no inertial range at low resolution. In this $\mathcal{M} \approx 7.0$ run, the velocity power spectrum is dominated by the solenoidal component, re-

sulting in a substantial shallowing of the spectrum that is apparent in the higher-resolution runs. At 512^3 , the slope of the spectrum over the interval $8 \leq kL/2\pi \leq 18$ is only slightly steeper than $P(k) \propto k^{-4/3}$ for the velocity and its solenoidal (Figure 12) component. We find spectral slopes in two independent 512^3 simulations (whose power spectra were averaged together to give that plotted in the figures) that agree to within a few percent, suggesting that our time-averaging to obtain a reliable spectral slope.

Although we do not have a sufficiently long time-average to find a robust fit to the slope of the 1024^3 run, the slopes appear to be very similar. As before, the slope we have found is much shallower than is typically predicted for the inertial range, while being steeper than that presented in K07 as the bottleneck spectral slope. We note that in the MHD case, the range over which we find a power law seems to increase with resolution, which one would not expect if the feature was due to numerical dissipation (bottleneck).

It has been argued by K07 that the quantity $\mathbf{u} = \rho^{1/3}\mathbf{v}$ should have an inertial range power law of $k^{-5/3}$ even for supersonic turbulence, but we see over a wide range of wavenumbers a $k^{-4/3}$ law (Figure 13). Kurien et al. (2004) have shown for subsonic turbulence that, while the $k^{-5/3}$ law is appropriate when the energy timescale dominates over the helicity timescale, a $k^{-4/3}$ law is expected when the helicity timescale is non-negligible compared to the energy timescale, even when the relative helicity may seem insignificant. This should be investigated as a possible cause of the bottleneck effect in supersonic turbulence.

Over the range $10 \leq kL/2\pi \leq 18$, the compressive component (Figure 14) of the 512^3 run follows a power law $P(k) \propto k^{-2.1}$. For 1024^3 run, the power spectrum appears to smoothly change slope, indicating that it is not a power law, but a longer time-average might change the shape. The power spectrum of the magnetic field at 512^3 follows the power law $P(k) \propto k^{-1.2}$ over the range $8 \leq kL/2\pi \leq 18$. At 1024^3 , the slope appears very similar, but with extra noise at the smaller wavenumbers due to the short time-average used. For all resolutions studied, the uncompensated power approaches a constant, non-zero value at the highest wavenumbers. This produces a very prominent upturn in the compensated spectra.

A direct comparison for strong-field MHD with $k_{\text{pk}}L/2\pi = 8$ shows more power at high wavenumber from Athena than from ZEUS for the velocity and its compressive and solenoidal components, just as was true for the hydro case. If the shallowing of our velocity spectrum is due to the bottleneck effect, then what appeared to be inertial range when V03 was published is likely affected by the bottleneck as well.

Figure 16 shows our cylindrically-integrated power spectra at 512^3 . We find anisotropy in the power spectrum of magnetic field perturbations as well as the velocity and its solenoidal component. There is more power perpendicular to the mean magnetic field at a given wavenumber than parallel to it. Parallel to the mean field, the power law is roughly k^{-2} , similar to that of the purely hydrodynamic case. Perpendicular to the field,

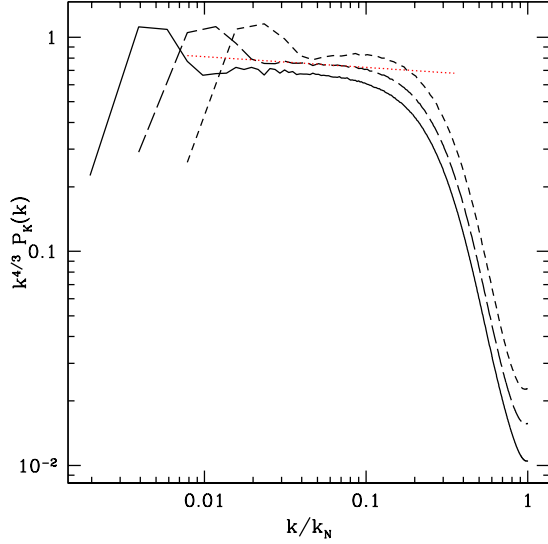


FIG. 11.— Spherically-integrated, compensated power spectra of the velocity for driven strong-field MHD turbulence runs with $k_{pk}L/2\pi = 2$ at 1024^3 (solid), 512^3 (long dashed), and 256^3 (short dashed). The x-axis has been renormalized to give $k/k_N = 1$. Also shown is a fit (dotted) to the slope of the 512^3 run over the range $8 \leq kL/2\pi \leq 18$, $P(k) \propto k^{-1.38}$. The 1024^3 run appears only slightly steeper.

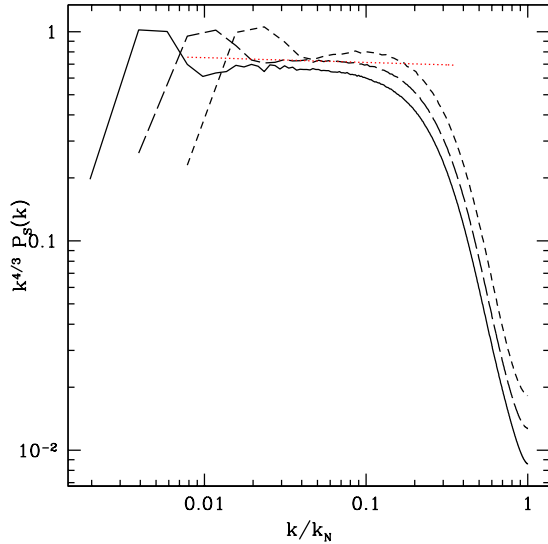


FIG. 12.— Spherically-integrated, compensated power spectra of the solenoidal component of velocity for driven strong-field MHD turbulence runs with $k_{pk}L/2\pi = 2$ at 1024^3 (solid), 512^3 (long dashed), and 256^3 (short dashed). The x-axis has been renormalized to give $k/k_N = 1$. Also shown is a fit (dotted) to the slope of the 512^3 run over the range $8 \leq kL/2\pi \leq 18$, $P(k) \propto k^{-1.36}$. The 1024^3 run appears only slightly steeper.

however, the slope is much more shallow, roughly $k^{-4/3}$. We find the power spectrum of the compressive component of velocity to be nearly isotropic, in contradiction to what was found in V03.

The velocity power spectrum of *subsonic* turbulence results from a conservative cascade of energy from large to small scales through interactions local in Fourier space. It is commonly believed that the velocity spectrum of supersonic turbulence, because it too is a power law, must also result from such a cascade. It is commonly known,

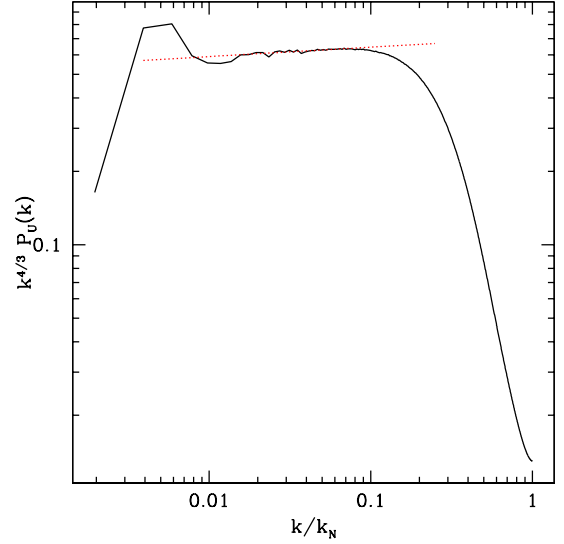


FIG. 13.— Spherically-integrated, compensated power spectra of the quantity $u = \rho^{1/3}v$ for driven strong-field MHD turbulence with $k_{pk}L/2\pi = 2$ at 1024^3 (solid). The x-axis has been renormalized to give $k/k_N = 1$. Also shown is a fit (dotted) to the slope over the range $8 \leq kL/2\pi \leq 36$, $P(k) \propto k^{-1.29}$.

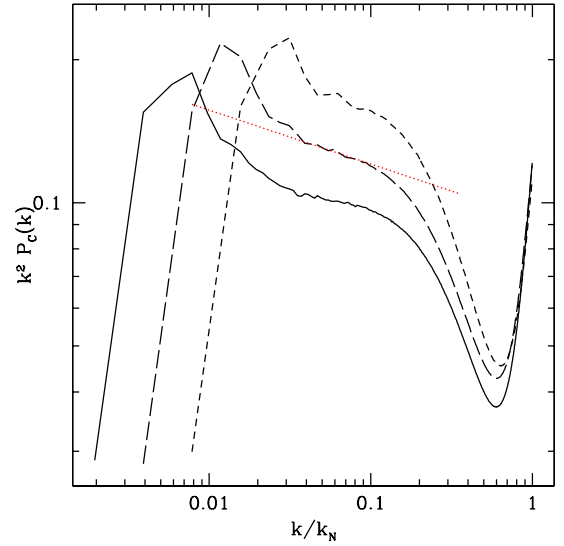


FIG. 14.— Spherically-integrated, compensated power spectra of the compressive component of velocity for driven strong-field MHD turbulence runs with $k_{pk}L/2\pi = 2$ at 1024^3 (solid), 512^3 (long dashed), and 256^3 (short dashed). The x-axis has been renormalized to give $k/k_N = 1$. Also shown is a fit (dotted) to the slope of the 512^3 run over the range $10 \leq kL/2\pi \leq 18$, $P(k) \propto k^{-2.11}$. The 1024^3 run, which does not have a sufficiently long time-average to be robust, does not appear to have power law form. The prominent upturn at the highest wavenumbers is due to the uncompensated power spectrum flattening out to a constant value.

however, that the power spectrum of a discontinuity, or an ensemble of shocks as in Burgers turbulence, also have velocity spectra that follow a power law, $P(k) \propto k^{-2}$. In Figure 17, we confirm that the compressive component of velocity in our 256^3 supersonic, strong-field MHD turbulence run with $k_{pk}L/2\pi = 2$ has a spectrum similar to that of velocity in an MHD blast wave that was initially spherical. This calls into question the long-held assumption that the power spectrum seen in supersonic turbu-

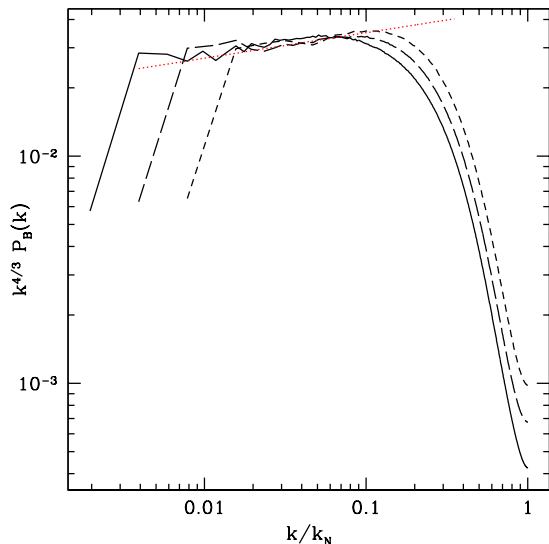


FIG. 15.— Spherically-integrated, compensated power spectra of the magnetic field perturbations for driven strong-field MHD turbulence runs with $k_{\text{pk}}L/2\pi = 2$ at 1024^3 (solid), 512^3 (long dashed), and 256^3 (short dashed). The x-axis has been renormalized to give $k/k_N = 1$. Also shown is a fit (dotted) to the slope of the 512^3 run over the range $8 \leq kL/2\pi \leq 18$, $P(k) \propto k^{-1.22}$.

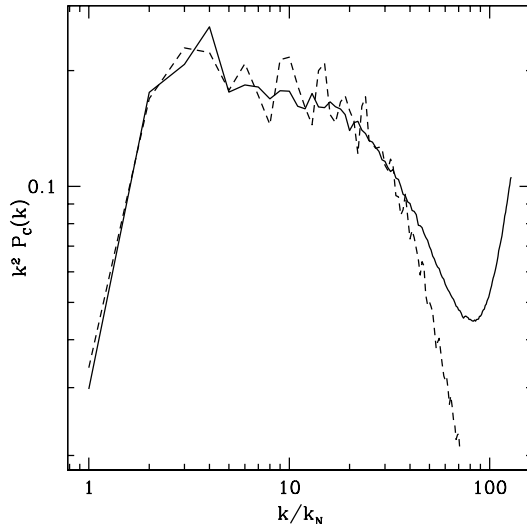


FIG. 17.— Spherically-integrated compensated power spectrum of the compressive component of velocity from one snapshot of the 256^3 driven strong-field MHD turbulence run (solid) shown in Figure 11, compared to the total velocity power spectrum of an initially-spherical MHD blast wave (short dashed), also at 256^3 . Except for the oscillations, the shapes of these spectra look quite similar between the driving and dissipative scales.

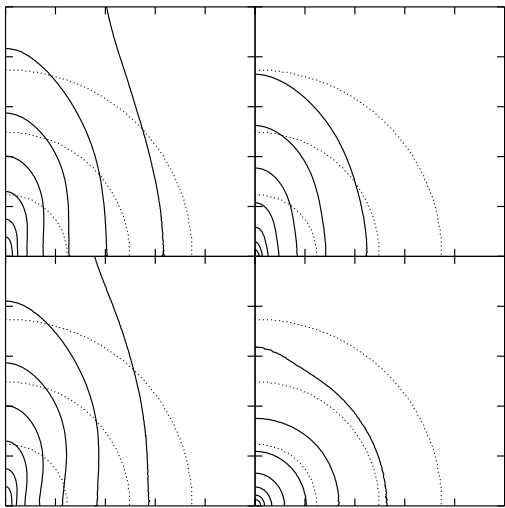


FIG. 16.— Cylindrically-integrated (uncompensated) power spectra (solid) of (a) the velocity, (b) the magnetic field, and the (c) solenoidal and (d) compressive components of velocity for the driven strong-field MHD turbulence run at 512^3 shown in Figure 11. The x and y axes are $k_{||}/k_N$ and k_{\perp}/k_N , respectively. The colors correspond to $P_K(k_{||}, k_{\perp})$, where $k^2 = k_{||}^2 + k_{\perp}^2$. Also shown for reference are circular contours (dotted).

lence results from an energy cascade facilitated by interactions local in Fourier space. It would seem that other diagnostics, such as structure functions, are necessary in order to determine the cause of the power law spectrum, either a Fourier-space cascade as in incompressible turbulence, or an ensemble of shocks as in Burgers turbulence.

To get a clearer idea of which features in our power spectra are representative of the turbulence and which were introduced in the post-processing, we compare power spectra computed by multiple methods. Our con-

trol spectrum will be computed as were the others presented in this section—averaged over the cells within a shell and then multiplied by the volume of the shell, $dV = 4\pi k^2 dk$, which we will refer to as “shell-averaged” for the remainder of this section. Our comparison will be to another commonly used method (e.g. P07), where the power is simply summed over the cells falling within the shell (“shell-summed”). These methods differ due to the discretization of the grid, i.e. because the Fourier-space volume occupied by the cells within a bin is not, in general, equal to the volume of the perfectly spherical shell that the bin represents. While the bins in our control spectrum are centered on integer values of $kL/2\pi$, those in the alternative spectrum instead run *between* integer values.

We use the time-averaged power spectrum of the driven strong-field MHD turbulence run at 512^3 for our comparison, although the effect should be independent of the run being analyzed. When overplotting the spectra produced by these two methods (see Figure 18), the most obvious difference is at low k . Although the shell-averaged spectrum is relatively smooth in the range $5 < kL/2\pi < 20$, the other has a jagged shape over this same range resulting from its sensitivity to the number of cells falling within a bin, making the “slope” of the power spectrum in this region much less obvious.

If we compare the shell-summed spectrum to one computed by the same method but with the bins shifted by half a bin width (aligning these bins with our own), we find that shape of the spectrum at low k changes considerably. If, on the other hand, we take the shell-averaged spectrum and compare it to one computed in the same manner but with bins shifted to align with those typically used in the shell-summed method, we see that, although the power in each bin does change, the shape and slope of the spectrum change very little. While neither method is right or wrong, we advise caution when

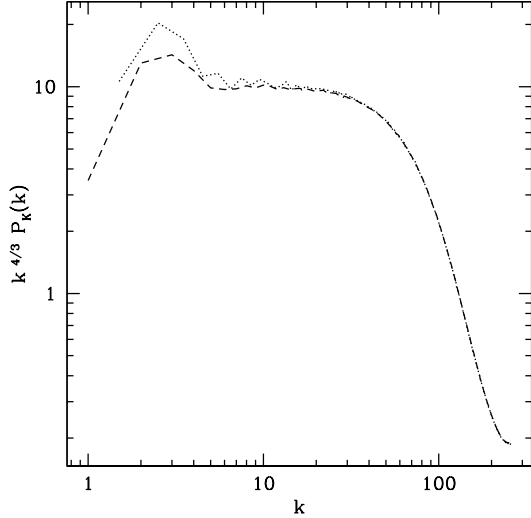


FIG. 18.— Spherically-integrated compensated power spectrum of the total velocity for the 512^3 driven strong-field MHD turbulence run shown in Figure 11 calculated using our standard method (solid) compared to the method described in P07 (dotted). The PS computed using the P07 method is more jagged in the range $5 < kL/2\pi < 20$. Note that the compensation used for this pair of power spectra is non-standard.

choosing a binning method for power spectra; differences in slope computed by different means are not necessarily indicative of different turbulent states.

3.3. Sonic Scale

Although molecular clouds have supersonic velocity dispersions on large scales, as one looks to smaller and smaller scales, turbulent compressions will become progressively weaker, at some point becoming subsonic. The length scale at which the RMS velocity dispersion is equal to the sound speed is referred to as the sonic scale (McKee & Ostriker 2007). We now investigate how the velocity dispersion varies on spatial scales larger than the sonic scale, where shocks are most important. This scaling can be determined observationally in the form of linewidth-size relations using many different methods. For example, Brunt (2003) used principal component analysis (PCA) to determine the linewidth-size relation within individual clouds.

To determine the velocity dispersion at a given length scale, $kL/2\pi = m$, where $m = 2^n$ and n is an integer, we divide our computational domain along each axis into m sections, yielding m^3 sub-volumes. We compute the velocity dispersion in each sub-volume and then average over all sub-volumes at that scale. Because crossing the sonic scale represents a change in the physics dominating the flow, i.e. waves steepening to form shocks, for this analysis only we will compute the velocity dispersion without mass-weighting, i.e. $\sigma_v = [\sigma_{v_x}^2 + \sigma_{v_y}^2 + \sigma_{v_z}^2]^{1/2}$, where $\sigma_{v_i} = [\langle v_i^2 \rangle - \langle v_i \rangle^2]^{1/2}$.

Figure 19 shows the velocity dispersion versus length scale for the 1024^3 , $\mathcal{M} \sim 7$ driven hydrodynamic turbulence run with $k_{pk}L/2\pi = 2$. Since driving may affect the scaling relation, we truncate our driving spectrum at $kL/2\pi = 8$, where the driving has already dropped to only 1% of the peak level, and consider only this and smaller scales. Fitting to the data points falling between

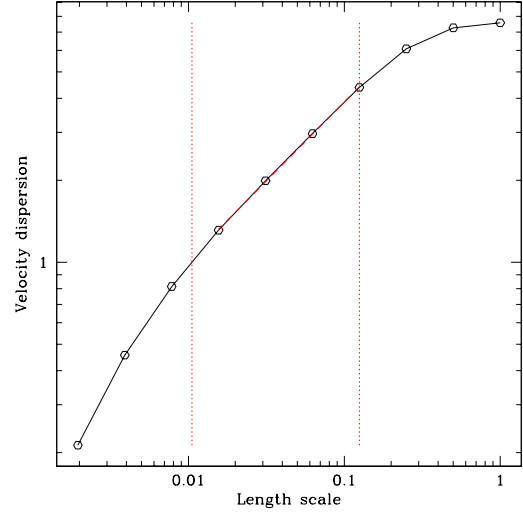


FIG. 19.— 3D velocity dispersion versus the spatial scale on which it is measured for driven hydrodynamic turbulence with $k_{pk}L/2\pi = 2$ (open hexagons). Also shown is a power law fit, $\sigma_l \propto l^{0.58}$, from the driving cutoff ($kL/2\pi = 8$) down to our last data point above the sonic scale (both limits marked with dashed lines). We have connected our data points with a solid line to make comparing to the fit easier.

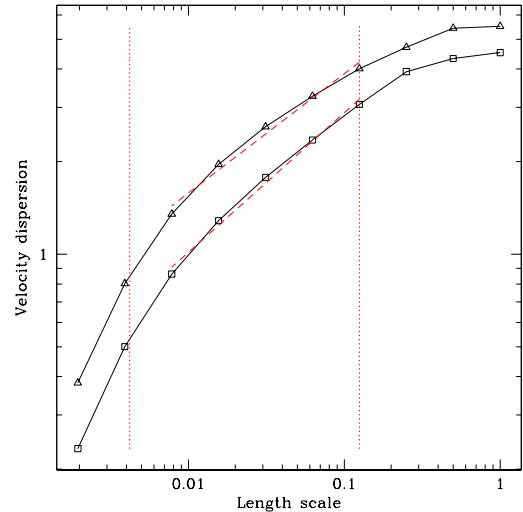


FIG. 20.— 1D velocity dispersion parallel to the magnetic field (open squares) and 2D velocity dispersion perpendicular to the field (open triangles) versus the spatial scale on which it is measured for driven strong-field MHD turbulence with $k_{pk}L/2\pi = 2$. From the driving cutoff ($kL/2\pi = 8$) down to our last data point before the 3D velocity dispersion becomes subsonic (both marked with dashed lines), neither the parallel nor perpendicular velocity dispersion has power law form (dotted). We have connected our data points with a solid line to make comparing to the power laws easier.

the sonic scale and the driving cutoff, a factor of eight in length, we find a clear power law of the form $v(l) \propto l^{0.58}$. This scaling index falls well within the range of indices found observationally by Brunt (2003).

Shown in Figure 20 is the velocity dispersion versus length scale for the 1024^3 , $\mathcal{M} \sim 7$ driven strong-field MHD turbulence run with $k_{pk}L/2\pi = 2$. This time, over the range of scales where the flow is supersonic, we find

that the slope is not a power law. Unlike in hydrodynamic turbulence, the sonic scale is not the only scale at which the dominant physics changes. In fact, we would expect the multiple wave families of MHD to lead to multiple transitions, and for strong fields, these transitions are widely separated. For example, parallel to the magnetic field, slow waves will travel at the sound speed, whereas fast waves will travel at the Alfvén speed. Perpendicular to the field, however, the slow waves will have zero velocity and the fast waves will travel with a speed $\sqrt{v_A^2 + c_s^2}$. This is complicated further by the fact that the parallel and perpendicular directions are defined relative to the *local* magnetic field, not the mean field. As a result, we have no reason to expect a uniform power law between the sonic scale and driving cutoff. It is not clear to what extent this result is affected by dissipation.

3.4. Time-variability and Temperature Intermittency

Up to this point we have averaged quantities from multiple snapshots in order to minimize the effect of rare events on our results. Our final set of diagnostics will instead be an analysis of the time-variability and temperature intermittency of the turbulent gas.

3.4.1. Saturation Amplitude

We begin by analyzing the time-variability of some of the quantities we analyzed in §3.1. For our hydrodynamic runs with the smallest driving scale, $k_{\text{pk}}L/2\pi = 8$, we find the time-variability of the saturation energy to be only half a percent at both 256^3 and 512^3 . Time-variability of less than a percent agrees with the results in S98 even though they drove their turbulence impulsively. The time-variability quoted in K07, however, is much higher. The K07 runs were driven at a much larger driving scale than our own. To investigate if this could be the reason for the discrepancy, we will also analyze the time-variability of our runs with larger driving scales.

When we increase the driving scale to $k_{\text{pk}}L/2\pi = 4$, we find the time-variability of the energy to be a full percent at both 256^3 and 512^3 . As both the driving scale and Mach number are varied here as compared to the run we discussed above, this could be due to either. When we increase the driving scale further, to $k_{\text{pk}}L/2\pi = 2$, without changing the Mach number, we find the time-variability increases yet again, coming to 2% at 256^3 and approaching 4% at 512^3 . It would seem that the driving scale chosen has a significant impact on the time-variability of the energy. The values we find here are still less than that shown in the K07 figure, however.

For strong-field MHD, we again find time-variability of about half a percent for the $k_{\text{pk}}L/2\pi = 8$ runs. Increasing the driving scale to $k_{\text{pk}}L/2\pi = 4$ decreases the time-variability at 256^3 but increases it a small amount at 512^3 . Increasing the driving scale further, to $k_{\text{pk}}L/2\pi = 2$, yields time-variability of 3% at 256^3 and 4% at 512^3 , comparable to the hydro runs.

When we compare the time-variability of the energy among hydro runs at 512^3 with varied Mach number that are driven at $k_{\text{pk}}L/2\pi = 4$, we find that the relation is non-monotonic. With $k_{\text{pk}}L/2\pi = 2$, however, we do see a monotonic relationship, with the time-variability increasing with Mach number. For our strong-field MHD runs, we again find non-monotonicity at $k_{\text{pk}}L/2\pi = 4$,

while the time-variability increases with Mach number at $k_{\text{pk}}L/2\pi = 2$, with the exception of the lowest Mach number run.

3.4.2. Temperature Intermittency

A feature of turbulence that may have a strong influence on star formation is intermittency, dissipation that is highly localized in space and time (McKee & Ostriker 2007). Although such dissipation does not require shocks, it is worthwhile to study the shock contribution in supersonic turbulence. Were we not assuming an isothermal equation of state, energy dissipation in these regions would lead to local heating and thus increased temperatures, which would be evident in observations. Therefore, to study intermittency due to shocks, we analyze the maximum heating rate per unit mass, $Q = c_s^2 \nabla \cdot \mathbf{v}$, a surrogate for temperature.

Since we expect the maximum heating rate, Q_{max} , to be strongly influenced by rare events, such as the interaction of multiple shocks, we consider the time-variability of this quantity. Due to the discretization of the grid, however, we would expect a component of the time-variability to be due to grid-scale fluctuations. Therefore, instead of considering Q_{max} directly, we consider the statistics of the high- Q tail of the PDF of the heating rate per unit mass. For each simulation that we consider, we compute the heating rate per unit mass, Q , in each cell over many snapshots. Considering only the cells in each snapshot that compose the 1% of material (by mass or volume) with the highest cell-averaged Q , we compute the mean value. Following the time-variability of this value should allow us to ignore meaningless grid-scale fluctuations while studying the intermittency due to shocks.

For driven hydrodynamic turbulence at 512^3 , we find the low Mach number runs driven at $k_{\text{pk}}L/2\pi = 4$ to have less than 1% variability in the peak temperature, while the higher Mach number runs with this same driving scale can have variability as large as 2% but without a monotonic dependence on Mach number. At the larger driving scale $k_{\text{pk}}L/2\pi = 2$, however, the variability in the peak temperature always exceeds 1% and can be as high as 4%. It would seem that this, like the time-variability of the saturation energies, increases with driving scale. For our runs, the variability of the peak temperature as measured by the top 1% of the volume never exceeds that from the top 1% of the mass by more than a tiny amount. As we have very few data dumps with which to calculate the statistics, however, the quantitative behavior may not be robust.

We find that, in 512^3 strong-field MHD turbulence driven at $k_{\text{pk}}L/2\pi = 2$, the variability of the peak temperature can be as large as 9%. When driven at $k_{\text{pk}}L/2\pi = 4$, however, the variability always decreases, never exceeding 3%. The variability measured by the top 1% of mass is typically larger than that from the top 1% of volume, but there does not appear to be a strong dependence on Mach number. More often than not, the variability in the strong-field MHD runs are larger than in the hydro runs at the same Mach number. Again, however, these statistics are computed from very few data dumps, making them subject to large errors. Figure 21 shows the time-evolution of the peak temperature in the $k_{\text{pk}}L/2\pi = 4$ strong-field MHD run with

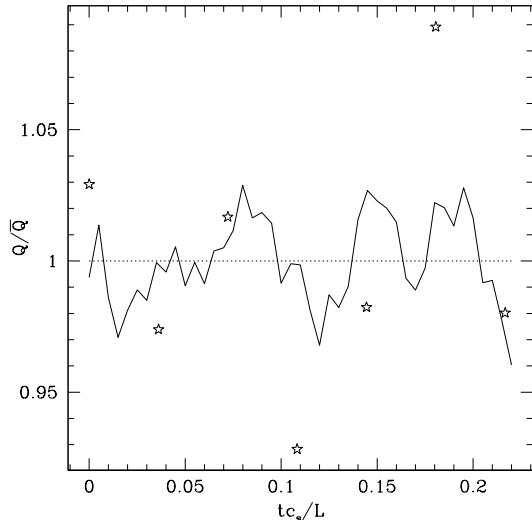


FIG. 21.— Maximum heating rate per unit mass (solid), where the tail (see §3.4.2) is defined by the top 1% of mass, for driven strong-field $\mathcal{M} \sim 7$ MHD turbulence with $k_{\text{pk}}L/2\pi = 4$ at 512^3 . The time-variability here is lower compared to the case where $k_{\text{pk}}L/2\pi = 2$ (shown by stars) at roughly the same Mach number.

$\dot{E}/\bar{\rho}L^2c_s^3 = 1000$, for which we have better than typical statistics, compared to the $k_{\text{pk}}L/2\pi = 2$ run with $\dot{E}/\bar{\rho}L^2c_s^3 = 500$.

4. DISCUSSION AND CONCLUSIONS

The saturation energies and dissipation timescales we find support the conclusion of S98 that supersonic turbulence dissipates rapidly even in the presence of magnetic fields. The results of our Godunov code agree with ZEUS, an operator-split method that relies on artificial viscosity to capture shocks, but reach convergence at slightly lower resolutions. At 512^3 the difference in the total energy in fluctuations between Athena and ZEUS for strong-field MHD is very small, indicating that these two codes converge to similar turbulent states at sufficiently high resolution.

The convergence resolution of our simulations depends both on the driving scale and the presence of a magnetic field. While hydro turbulence driven at $k_{\text{pk}}L/2\pi = 4$ converges by 64^3 , strong-field MHD turbulence driven at $k_{\text{pk}}L/2\pi = 8$ does not converge until 512^3 . Although very high resolutions are needed to capture the inertial range of the turbulence, lower resolutions are often adequate for studying the energy dissipation characteristics of the turbulence as well as other volume-integrated quantities.

At high Mach number, the ratio of the dissipation timescale to the flow crossing time at the driving scale increases with increasing magnetic field strength; however, it does not exceed unity even for strong-field MHD turbulence. This ratio is independent of driving scale. The fractions of the kinetic energy in solenoidal and compressive modes are also independent of driving scale, with the compressive fraction generally being more than twice as high for hydrodynamic than for strong-field MHD turbulence.

Our spherically-integrated velocity power spectra for decaying, subsonic hydrodynamic turbulence show evi-

dence of the bottleneck effect in the velocity power spectrum, consistent with the findings of Sytine et al. (2000). We find more power at high wavenumber in our driven, supersonic hydro and MHD turbulence simulations than was found by V03, but it is unclear, particularly in the MHD case, whether or not this is due to a bottleneck. Resolutions exceeding 1024^3 will be necessary to draw firm conclusions about the slope of the inertial range. The cylindrically-averaged velocity power spectrum for driven MHD turbulence is very anisotropic; it has a slope that approximates that of the hydrodynamic case parallel to the magnetic field, while perpendicular to the field it is much more shallow. The compressive component of velocity has an isotropic power spectrum, contrary to what was found in V03.

We find the compressive component of velocity in driven, supersonic MHD turbulence to have a power spectrum that is difficult to distinguish from the velocity spectrum of an initially-spherical MHD blast wave. This calls into question the long-held assumption that supersonic turbulence power spectra result from an energy cascade facilitated by interactions local in Fourier space. The analysis of structure functions may be useful in determining the source of the power law spectrum in supersonic turbulence, either a Fourier-space cascade as in incompressible turbulence, or an ensemble of shocks as in Burgers turbulence.

For hydrodynamic turbulence, we find a power law scaling of the velocity dispersion with spatial scale, $\sigma(l) \propto l^{0.58}$, for scales where the velocity dispersion is supersonic. However, we find no such power law for strong-field MHD turbulence, where the sonic scale is not the only scale of interest. In this case, we find that the velocity dispersion drops off more rapidly than a power law as one approaches smaller scales.

We see time-variability in the saturation energies comparable to that of the equivalent runs in S98 despite the impulsive driving employed therein. Our time-variability increases when we apply our turbulent driving at larger scales, but remains lower than that shown in K07 even with $k_{\text{pk}}L/2\pi = 2$. It is possible that the acceleration-based driving method of K07 is responsible for the difference. At this large driving scale, the time-variability increases with Mach number for both hydro and strong-field MHD. The method used to drive the turbulence appears to have a substantial impact on the resulting turbulent state.

Further investigation should be conducted to determine how much of the increase in time-variability with driving scale is due to the limited range of scales over which an inverse cascade can occur. If the level of time-variability is determined to be a result of simulation setup and not representative of the physical system we are trying to simulate, better diagnostics or simulation methods need to be developed in order to quantify intermittency in turbulent media. Although we have very poor statistics in our temperature intermittency analysis, it appears that this, too, increases with driving scale. Considering the difference that the driving method makes on the results, it may be more realistic to study decaying turbulence instead of driving it arbitrarily.

For identical turbulent data cubes, we find that the post-processing methods chosen significantly influence the results. The turbulent Mach number changes by

$\sim 4\%$ depending on the method used in its computation. The means of computing the power spectrum also has a strong influence on the power at wavenumbers overlapping with the inertial range. When comparing results published by different groups, one should keep in mind that this, as well as the code, driving method, and initial conditions, can affect the quantities being compared.

Although the saturation energies and energy dissipation characteristics of the turbulence converge at resolutions within our current computational capabilities, the power spectra appear to require much higher resolutions to provide valuable information. Also considering that turbulent power spectra can be approximated by non-turbulent phenomena, it would seem that, for the time being, our focus should be on other diagnostics.

In conducting these numerical simulations, we have made many simplifications in order to make the problem

more tractable. These assumptions, however, may prove to significantly impact the results. Future studies should consider non-ideal MHD in order to model low-ionization molecular clouds, a non-isothermal equation of state in order to study heating and cooling, and self-gravity in order to follow the collapse of the bound clumps that form in the turbulent medium.

We thank Eve Ostriker for very productive discussion and Tom Gardiner for his invaluable assistance in bringing Athena up to the task of successfully simulating supersonic turbulence. We would also like to thank Alexei Kritsuk, Cristoph Federrath, and Alex Lazarian for their feedback. Simulations were performed on the IBM Blue Gene at Princeton and on computational facilities supported by NSF grants AST-0216105 and AST-0722479.

APPENDIX

SUPERSONIC TURBULENCE WITH GODUNOV SCHEMES

The calculations presented in this paper were conducted using Athena, a directionally-unsplit, higher-order Godunov code. This code exactly conserves mass, momentum, and magnetic flux, as well as energy when assuming an adiabatic equation of state. The code captures shocks well and has a low level of numerical dissipation. Although the full details of the algorithms and implementation can be found in the literature (Gardiner & Stone 2005, 2008; Stone et al. 2008; Stone & Gardiner 2008), we will briefly summarize here, noting any modifications made to the algorithms in order to successfully run the challenging problem of high Mach number turbulence.

The integration algorithm used in our calculations is a simple predictor-corrector scheme based on the MUSCL-Hancock scheme of van Leer (2006), combined with the constrained transport method of Evans & Hawley (1998) to enforce the divergence-free constraint on the magnetic field (i.e. the VL+CT algorithm described in detail in Stone & Gardiner 2008). We find the additional diffusion associated with this scheme as compared to our CTU+CT algorithm (described in detail in Stone et al. 2008) to make it more robust to the strong rarefactions that arise in a highly turbulent medium. Although the algorithm is formally only second-order accurate, we use third order (piecewise parabolic) spatial reconstruction, finding it to provide more accurate solutions in test problems due to smaller truncation error.

For our isothermal hydrodynamics runs, we found there to be strong rarefactions within the turbulent medium for which an approximate Riemann solver simply was not accurate enough, necessitating the use of an exact nonlinear Riemann solver. For adiabatic hydrodynamics as well as isothermal and adiabatic MHD, we were able to use approximate nonlinear Riemann solvers, namely HLLC for the hydro case and HLLD for MHD, more details about which can be found in Stone et al. (2008). Although we used our own adaptation of the adiabatic HLLD solver of Miyoshi & Kusano (2005) for our isothermal MHD runs, we found it to produce turbulent states extremely similar to those from the isothermal HLLD solver of Mignone (2007).

Although these Riemann solvers are positive definite in 1D, it is not guaranteed that they will be so in multidimensions. In fact, we found that, under extreme conditions, the net mass flux out of a cell in our isothermal 3D turbulent medium occasionally exceeded the cell's initial mass. In the rare circumstance that this occurred, we recomputed the fluxes of all variables through all interfaces bordering such cells using first-order reconstruction. In our Mach 7 strong-field MHD run at 512^3 that uses $k_{\text{pk}}L/2\pi = 2$, this affected only a fraction 3×10^{-10} of the fluxes computed in the corrector step of the integrator. Dropping to first order introduced enough diffusion in the immediate vicinity to keep the cell-averaged density positive, while having a negligible effect on the overall system. Adding diffusion in this manner instead of enforcing a density floor maintains exact conservation.

REFERENCES

- Brunt, C.M. 2003, *ApJ* 584, 293
- Cho, J. & Lazarian, A. 2003, *MNRAS* 345, 325
- Cho, J. & Lazarian, A. 2005, *ThCFD* 19, 127
- Churchwell, E. et al. 2004, *ApJS* 154, 322
- Crutcher, R.M. 1999, *ApJ* 520, 706
- Elmegreen, B.G. & Scalo, J. 2004, *ARAA* 42, 211
- Esquivel, A., Lazarian, A., & Pogosyan, D. 2003, *MNRAS* 342, 325
- Evans, C.R. & Hawley, J.F. 1988, *ApJ* 322, 659
- Falgarone, E., & Philips, T.G. 1990, *ApJ* 359, 344
- Federrath, C., Klessen, R.S., & Schmidt, W. 2008, in prep.
- Gardiner, T.A. & Stone, J.M. 2005, *JCoPh* 205, 509
- Gardiner, T.A. & Stone, J.M. 2008, *JCoPh* 227, 4123
- Haugen, N.E.L. & Brandenburg, A. 2004, *PhRvE* 70, 026405
- Kowal, G., Lazarian, A., & Beresnyak, A. 2007, *ApJ* 658, 423
- Kritsuk, A.G., Norman, M.L., Padoan, P., & Wagner, R. 2007, *ApJ* 665, 416 (K07)
- Kurien, S., Taylor, M.A., & Matsumoto, T. 2004, *PhRvE* 69, 066313
- Lemaster, M.N. & Stone, J.M. 2008, *ApJL* 682, L97 (Paper I)
- Mac Low, M.-M. 1999, *ApJ* 524, 169
- Mac Low, M.-M. & Klessen, R.S. 2004, *RvMP* 76, 125
- McKee, C.F. & Ostriker, E.C. 2007, *ARAA* 45, 565
- Mignone, A. 2007, *JCoPh* 225, 1427
- Miyoshi, T. & Kusano, K. 2005, *JCoPh* 315, 344
- Mizuno, A., Onishi, T., Yonekura, Y., Nagahama, T., Ogawa, H., & Fukui, Y. 1995, *ApJ* 445, L161
- Ostriker, E.C., Gammie, C.F., & Stone, J.M. 1999, *ApJ* 513, 259
- Ostriker, E.C., Stone, J.M., & Gammie, C.F. 2001, *ApJ* 546, 980

- Padoan, P., Jones, B.J.T., & Nordlund, A.P. 1997, ApJ 474, 730
- Padoan, P., Nordlund, A., Kritsuk, A.G., Norman, M.L., & Li, P.S. 2007, ApJ 661, 972 (P07)
- Passot, T. & Vazquez-Semadeni, E. 1998, PhRvE, 58, 4501
- Porter, D., Pouquet, A., Sytine, I., & Woodward, P. 1999, PhyA 263, 263
- Press, W.H., Flannery, B.R., Teukolsky, S.A., & Vetterling, W.T. 1992, Numerical Recipes in C (2nd ed.; Cambridge: Cambridge University Press)
- Stone, J.M., & Gardiner, T.A. 2008, NewA, in press
- Stone, J.M., Ostriker, E.C., & Gammie, C.F. 1998, ApJ 508, L99 (S98)
- Stone, J.M., Gardiner, T.A., Teuben, P., Hawley, J.F., & Simon, J. 2008, ApJS, in press (arXiv0804.0402)
- Sytine, I.V., Porter, D.H., Woodward, P.R., Hodson, S.W., & Winkler, K.-H. 2000, JCoPh 158, 225
- van Leer, B. 2006, Comm. Comp. Phys. 1, 192
- Vestuto, J.G., Ostriker, E.C., & Stone, J.M. 2003, ApJ 590, 858 (V03)